© von Karman Institute for Fluid Dynamics
Waterloosteenweg 72 – 1640 Sint-Genesisu-Rode

Dear reader,

The electronic document attached is protected by copyright laws.

This article may be used for research, teaching and private study purposes. Any substantial or systematic reproduction, redistribution, reselling, loan, sub-licensing, systematic supply, or distribution in any form to anyone is expressly forbidden.

Please do not distribute the document to third parties outside your workgroup as under current copyright law it is only intended for your personal scientific use. If you do not comply with the above conditions of use, you may be held liable for copyright infringement.

VON KARMAN INSTITUTE FOR FLUID DYNAMICS

LECTURE SERIES 1984-03

DIGITAL IMAGE PROCESSING IN FLUID DYNAMICS

MARCH 5-9, 1984

OPTICAL PROCESSING

L. HESSELINK - STANFORD U., USA

OPTICAL PROCESSING

Prof. L. Hesselink
Stanford University
#377 Durand
Stanford, CA 94305-2186

March 1984

Introduction

The objective of this workshop is to present recent advances in modern optical methods and digital image processing related to Fluid Mechanics research. In this course we will advocate the approach of Fourier optics and classical instruments, such as a schlieren system, are analyzed using this approach. This analysis does not only provide a much better understanding of the physics involved than is usually covered in Fluid Mechanics textbooks, but it opens up new possibilities for research, in particular in the area of digital image processing. The speckle interferometer which is used to determine statistical quantities describing a random density field is a case in point. In the section on tomography the emphasis is focused on the understanding of the basic principles involved, the advantages and disadvantages of the different techniques and current interest in the field. Whenever possible pertinent references are provided as a guide to the recent literature.

The holography section is intended to outline the principle. The use of holography for 3-D data storage in emphasized and the role which holograms play in optical processors is indicated. Finally, several applications of these new techniques in the area of Fluid Mechanics are presented.

I. Concepts of modern optics

The use of Fourier transform techniques in the analysis of optical systems was stimulated to a large extent by a French scientist, P M Duffieux in the late 1930's. Today Fourier optics is a powerful tool in the analysis of systems using coherent and incoherent sources Here we will restrict ourselves to linear systems, i.e., the response of the system to several stimuli acting simultaneously is identically equal to the sum of the responses that each of the component stimuli would produce individually. This superposition principle was first clearly formulated by Huygens and is now known as the Huygens' principle Mathematically it can be formulated as follows:

$$E(x,y,\omega) \quad \iint K(x',y';x,y;\omega)\, E(x',y',\omega)\, dx'dy' \qquad (1)$$

where $E(x,y,\omega)$ denotes a field parameter with frequency ω say the electric field component of the electro-magnetic radiation in a plane (x,y) $E(x',y',\omega)$ represents the field in another plane (x',y') and $K(x',y';x,y;\omega)$ denotes a Kernel or weighting function describing the superposition The Kernel can be calculated from the wave equation using Greens functions. This approach was historically formulated for diffraction problems, first by Augustin Jean Fresnel in 1818 and later extended by Gustav Kirchhoff in 1882 and inconsistencies regarding the boundary conditions were pointed out and eliminated by Poincare in 1892 and Sommerfeld in 1894.

Consider the following configuration:

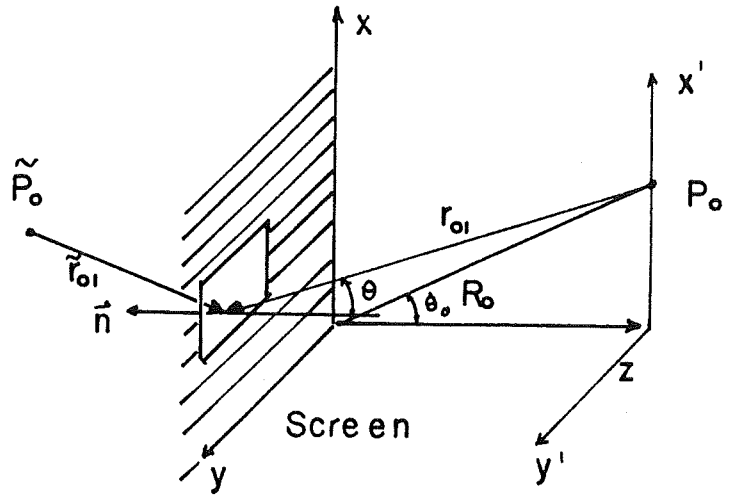


Figure (I. 1)

An expanding spherical wave emanating from $\tilde{P}_o$ illuminates the diffracting aperture Σ . The objective is to calculate the field in P_o , on the opposite side of the screen. The details of the calculation are clearly spelled out in Goodman (Ref. 1. 1) and only the result will be presented here:

$$E(P_o) = \frac{-1}{2\pi} \iint_{\Sigma} E(P_1) \left(jk - \frac{1}{r_{o1}}\right) \frac{\exp(jk r_{o1})}{r_{o1}} \cos(\theta_{o1})\, ds \qquad (1.2)$$

Rayleigh-Sommerfeld diffraction formula

Note: The time dependence $e^{-j\omega t}$ has been omitted in all formulas

This equation is the starting point of our discussion. For most applications one can make simplifying assumptions, two of which have become extremely useful; namely, Fresnel and Fraunhofer diffraction. It basically means that the field should not be measured very close (in some sense) near the aperture and the wavelength should be small compared with the dimension of the aperture. Furthermore, the edge

effects in the plane of the aperture are neglected and the field is assumed to be undisturbed inside the aperture and zero in the geometrical shadow at the plane of the screen (Kirchhoff approximation). Two more assumptions are customarily made:

$$\text{i)} \quad ik \gg \frac{1}{r_{01}}$$

$$\text{ii)} \quad \cos\theta_{01} \sim \cos\theta_0$$

Thus:

$$E(P_0) \approx \frac{1}{j\lambda} \frac{\cos\theta_0}{R_0} e^{jkR_0} \iint_{z=0} E(x, y, 0)\, e^{jk(r_{01} - R_0)} \tag{1.3}$$

The Fresnel approximation amounts to:

$$\begin{aligned} r_{01} &= \sqrt{z^2 + (x' - x)^2 + (y' - y)^2} \\ &= z \sqrt{1 - \left(\frac{x' - x}{z}\right)^2 + \left(\frac{y' - y}{z}\right)^2} \\ &\approx z \left[1 + \tfrac{1}{2}\left(\frac{x' - x}{z}\right)^2 + \tfrac{1}{2}\left(\frac{y' - y}{z}\right)^2\right] \end{aligned} \tag{1.4}$$

Note: $R_0 \approx z$

and

$$z^3 \gg \frac{\pi}{4\lambda} \left[(x' - x)^2 + (y' - y)^2\right]^2_{\max} \tag{1.5}$$

Fresnel approximation

The result is:

$$E(P_0) = E(x', y') = \frac{\exp(jkz)}{j\lambda z} \int_{-\infty}^{\infty} E(x, y, 0) \exp\left\{\frac{jk}{2z}\left[(x' - x)^2 + (y' - y)^2\right]\right\} dx\, dy \tag{1.6}$$

$\cos\theta_{01} \approx 1$, paraxial approximation

This integral is of the convolution type and can be rewritten as:

$$E(x',y') = \frac{\exp(jkz)}{j\lambda z} \exp\left[j\frac{k}{2z}(x'^2+y'^2)\right] \int_{-\infty}^{\infty}\int E(x,y,0)$$

$$\exp\left[j\frac{k}{2z}(x^2+y^2)\right] \exp\left[-j\frac{2\pi}{\lambda z}(x'x + y'y)\right] dx\, dy \qquad (1.7)$$

When the quadratic phase term can be neglected,

$$z \gg \frac{k(x^2+y^2)}{2} \qquad (1.8)$$

we deal with the Fraunhofer approximation and (1.6) reduces to a Fourier transform with spatial frequencies $f_x = \frac{x'}{\lambda z}$, $f_y = \frac{y'}{\lambda z}$

$$E(x',y') = \frac{\exp(jkz)}{j\lambda z} \exp\left[j\frac{k}{2z}(x'^2 + y'^2)\right]$$

$$\int_{-\infty}^{\infty}\int E(x,y,0) \exp\left[-j\frac{2\pi}{\lambda z}(x'x + y'y)\right] dx\, dy \qquad (1.9)$$

The Fresnel approximation can be used closest to the aperture provided (1.5) is satisfied and is commonly referred to as near field approximation The Fraunhofer approximation is useful in the far field provided (1.7) is satisfied.

The physical interpretation of equation (1.6) and (1.8) is most interesting. It shows that for a converging spherical wave ($E(x,y) \sim \exp\left[-j\frac{k}{2z}(x^2 + y^2)\right]$ at the focus) the quadratic phase factor in (1.6) disappears and equation (1.6) becomes identical to (1.8). This is a very important notion, and an example illustrating this point will be given here.

Consider the following:

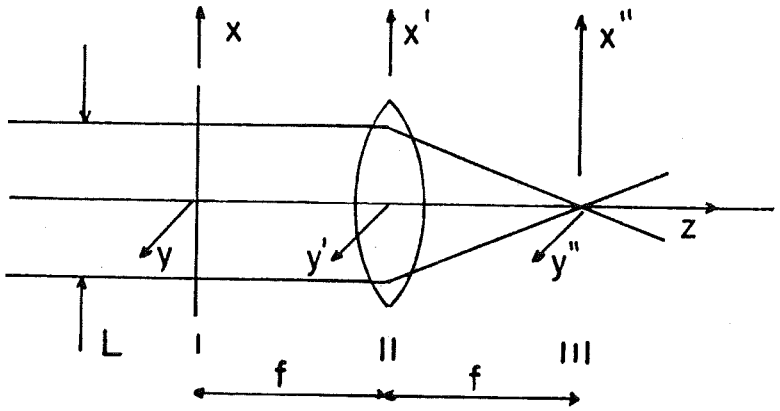


Figure I.2

A monochromatic normally incident plane wave of unit amplitude impinges upon a converging lens with focal length f. Suppose an aperture of size L limits the spatial extent of the beam a distance f in front of the lens. In principle we could have chosen the object distance to assume any value, but the distance f simplifies the mathematics without obscuring any of the principal physics.

First we propagate the field from plane I to II. At plane I the field amplitude, say the scalar electric field (for the moment we don't worry about Maxwell's equations and the coupling between electric and magnetic fields), has unit amplitude:

$$\begin{aligned} E = 1 \quad &\text{for} \quad x \le L/2 \quad \text{or} \quad P = 1 \\ &\qquad\quad y \le L/2 \\ E = 0 \quad &\text{for} \quad x > L/2 \quad \text{or} \quad P = 0 \\ &\qquad\quad y > L/2 \end{aligned} \tag{1.10}$$

We denote the aperture by $P(x,y)$, called the pupil function.

Using equation (1.7), the Fresnel approximation in the near field, which is in general valid more than 10 wavelengths away from the object, the field distribution is calculated just in front of the lens:

$$E_{up}(x',y') = \frac{\exp(jkf)}{j\lambda f} \exp\left[j\frac{k}{2f}(x'^2 + y'^2)\right]$$

$$\int_{-\infty}^{\infty}\int P(x,y)\exp\left[j\frac{k}{2f}(x^2+y^2)\right]\exp\left[-j\frac{2\pi}{\lambda f}(x'x+y'y)\right]dx\,dy \qquad (1.11)$$

The propagation through the lens is described by a transmission function $T(x',y')$. Assume that the lens is infinitesimally thin and therefore the field distribution just behind the lens can be calculated by multiplying $P(x,y)$ under the integral by $T(x',y')$ to give:

$$E_{down}(x',y') = \frac{\exp(jkf)}{j\lambda f} \exp\left[j\frac{k}{2f}(x'^2 + y'^2)\right]$$

$$\int_{-\infty}^{\infty}\int P(x,y)\,T(x',y')\exp\left[j\frac{k}{2f}(x^2+y^2)\right]\exp\left[-j\frac{2\pi}{\lambda f}(x'x + y'y)\right]dx\,dy \qquad (1.12)$$

Finally the propagation of the field from the lens to the back focal plane is calculated according to

$$E(x'',y'') = \frac{\exp(jkf)}{j\lambda f}\exp\left[j\frac{k}{2f}(x''^2+y''^2)\right]\int\int E(x',y')$$

$$\exp\left[j\frac{k}{2f}(x'^2 + y'^2)\right]\exp\left[-j\frac{2\pi}{\lambda f}(x'x'' + y'y'')\right]dx'\,dy' \qquad (1.13)$$

The amplitude transmission function for the lens is given by:

$$T(x', y') = P(x', y') \exp\left[- j \frac{k}{2f} (x'^2 + y'^2) \right] \tag{1.14}$$

Assume that the lens diameter is large compared with L, and therefore $P(x', y') = 1$ in (1.14). Upon substitution of (1.14) into (1.13) the quadratic phase factor under the integral disappears and

$$E(x'', y'') = \frac{\exp(jkf)}{j\lambda f} \exp\left[j \frac{k}{2f} (x''^2 + y''^2) \right] F\left\{ \frac{x''}{\lambda f} , \frac{y''}{\lambda f} \right\} \tag{1.15}$$

where $F\left\{ \frac{x''}{\lambda f} , \frac{y''}{\lambda f} \right\}$ denotes the Fourier transform of $E(x', y')$ evaluated at frequencies $\frac{x''}{\lambda f}$, $\frac{y''}{\lambda f}$.

Equation (1.11) is of the convolution type, as indicated in (1.6). Upon taking the Fourier transform of both sides of eq. (1.6) and neglecting the constant phase factor $\frac{\exp(jkz)}{j\lambda z}$ we get

$$\begin{aligned} F\{ E(x', y') \} &= F\{ E(x, y, 0) \} \exp\left[- \frac{j\pi}{\lambda f} (x^2 + y^2) \right] \\ &= F\left\{ \frac{x'}{\lambda f} , \frac{y'}{\lambda f} \right\} \end{aligned} \tag{1.16}$$

It is now evident that upon substitution of (1.16) into (1.15) the quadratic phase factor cancels:

$$\begin{aligned} E(x'', y'') &= F\{ E(x, y, 0) \} \\ = \frac{\exp(jkf)}{j\lambda f} &= \int_{-\infty}^{\infty} \iint E(x, y, 0) \exp\left[-j \frac{2\pi}{\lambda f} (x''x + y''y) \right] dx\, dy \end{aligned} \tag{1.17}$$

This phase factor in front of the integral represents the overall phase retardation that any spectral component of the signal undergoes as it propagates between the two planes which are separated by a distance f. More often than not one is interested in the energy or square of the amplitude and this factor disappears in the convolution process.

Equation (1.17) shows the important result that for an object placed in the front focal plane of the lens the amplitude distribution at the back focal plane is given by its Fourier transform. The transform must be evaluated at frequencies $f_x = \frac{x''}{\lambda f}$, $f_y = \frac{y''}{\lambda f}$ to give the proper scaling at the observation plane. As a simple example consider a one dimensional slit, placed a distance f in front of a lens, i.e.,

$$\begin{aligned} P(x,y) &= 1 && |x| \leq L/2 \\ & && -\infty < y < \infty \\ P(x,y) &= 0 && |x| > L/2 \end{aligned} \qquad (1.18)$$

or

$$P(x,y) = P(x) = \text{rect}\left(\frac{x}{L}\right)$$

where

$$\begin{aligned} \text{rect}\left(\frac{x}{L}\right) &= 1 && |x| \leq L/2 \\ &= 0 && \text{otherwise} \end{aligned} \qquad (1.19)$$

The Fourier transform of this function is

$$F\left\{\text{rect}\left(\frac{x}{L}\right)\right\} = \frac{L}{j\lambda f}\exp(jkf)\,\text{sinc}\left(\frac{L x'}{\lambda f}\right)$$

where $\text{sinc } x = \frac{\sin \pi x}{\pi x}$.

The intensity I_0 is given by

$$I(x'', y'') = \frac{L^2}{\lambda^2 f^2} \text{sinc}\left(\frac{L x}{\lambda f}\right)$$

Graphically the result is shown in figure (I.3).

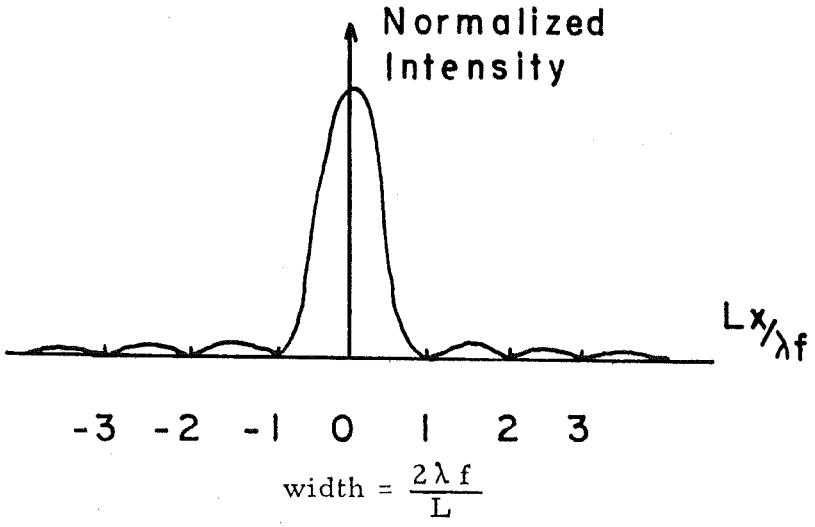


Figure (I.3). Fraunhofer diffraction pattern of a one-dimensional slit.

The result indicates the well-known principle of Fourier transforms, namely, that small scales in the object plane correspond to high frequencies in the Fourier transform plane. In other words, narrow slits produce wide diffraction patterns.

1.2

The rapidly increasing interest in optics, which started in the early sixties, is largely due to the invention of the laser. Three properties of this light source are responsible for its great practical use:

i) Radiation is emitted nearly monochromatically, and very narrow line widths are obtainable, i.e., long coherence lengths.

ii) The intensity of the radiation can be made very intense.

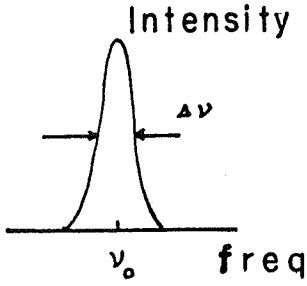
iii) Radiation is highly directional.

The principle of laser operation is treated in many textbooks, such as Lengyel (Ref.1.2), Siegman (Ref.1.3) and Yariv (Ref. 1.4), and will not be covered in detail here. However, some of the properties of lasers which are pertinent in the discussion of modern optical instruments will be briefly mentioned.

The laser consists of a resonant electromagnetic cavity within which an amplifying medium is positioned. Spontaneous emission in the amplifier medium is generated by electric discharge (flowing gas lasers) or optical pumping (f.i. flash lights in solid state lasers). The resonant radiation is emitted through either a small hole in one of the mirrors or a partially transmitting output mirror. The fundamental mode of the resonator has a Gaussian distribution in intensity and is designated by TEM_{oo} .

The line width of the monochromatic radiation is customarily quoted in units of $\Delta\nu$ or coherence length, ℓ .

$\ell \approx \frac{c}{\Delta\nu}$



where c is the speed of light and $\Delta\nu$ denotes the maximum frequency excursion during the time involved.

Figure I.4 Energy spectrum of a laser source.

To give an example, in an argon-ion laser the coherence length is typically of the order of 30 m during a 1 sec interval and 2 m over a period of an hour. The coherence length is of particular interest in interference phenomena, which will be treated in Section II. The power of laser radiation is quoted in W and the energy in J. For a c.w. argon-ion laser the intensity is typically between a few hundred mW/mm^2 and 10 - 20 W/mm^2. Lasers can be used in tandem, just as electronic amplifiers and extremely high energies be obtained. At Lawrence Livermore Radiation Laboratory energies of up to 10 kJ have been obtained in the fifteen stage, twenty beam neodimium glass laser amplifier circuit, in the SHIVA facility. (λ = 1.06 μm)

Using the terminology of Fourier optics, laser radiation is described by the following function:

$$E_x = A\, e^{-\frac{j\pi}{\lambda R}(x^2+y^2) - \frac{(x^2+y^2)}{w^2}} = A\, e^{-j\frac{\pi}{\lambda}(x^2+y^2)\left[\frac{1}{R}+\frac{1}{j\pi w^2}\right]}$$

$$= A\, e^{-\frac{j\pi}{\lambda\rho}(x^2+y^2)} \quad . \qquad (1.20)$$

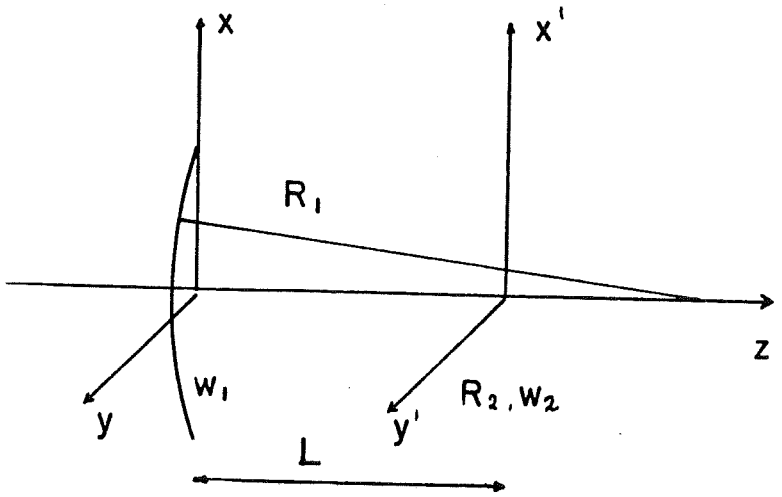


Figure I.5 Propagation of a Gaussian beam.

R: radius of curvature in plane I $\quad R < 0$ Divergent beam

$\quad R > 0$ Convergent beam

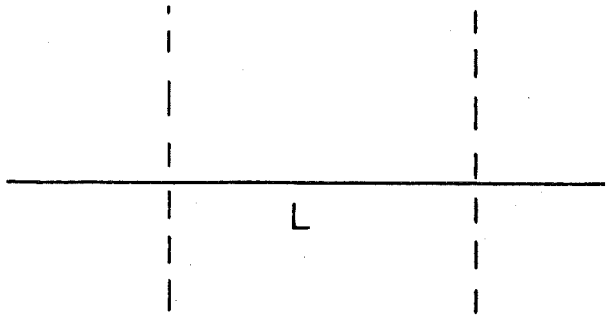
$$w = \sqrt{(x^2 = y^2)} \quad \text{and} \quad \left| E(x^2 + y^2 = w^2) \right| = \frac{1}{e} \left| E(0,0) \right| . \tag{1.21}$$

Define $\frac{1}{\rho} = \frac{-1}{R} + \frac{1}{\frac{j\pi}{\lambda} w^2}$.

Now substitute (1.20) in (1.6) and the result is:

$$E_x \approx \frac{e^{ikL - \frac{i\pi}{\lambda}[x^2 + y^2]/(\rho + L)}}{(\frac{1}{L} + \frac{1}{\rho})\ L} \tag{1.22}$$

In shorthand notation:



I II

Given: R, w

$$E_x = e^{-\frac{i\pi}{\lambda \rho_o}(x^2 + y^2)}$$

and

$$\frac{1}{\rho_o} = \frac{-1}{R} + \frac{1}{\frac{i\pi}{\lambda} w^2}$$

Calculate

$$E_x = e^{-\frac{i\pi}{\lambda \rho_{out}}(x^2 + y^2)}$$

$$\rho_{out} = \rho_o + L$$

$\frac{1}{\rho_o + L}$ = complex radius at the centerplane.

$$= \frac{-1}{R_2} + \frac{1}{\frac{i\pi}{\lambda} w_2^2}$$

$$= \frac{1}{\left(\frac{-1}{R_1} + \frac{1}{\frac{i\pi}{\lambda} w_1^2}\right)^{-1} + L}$$

$$= \frac{\frac{1}{R_1}\left(-1 + \frac{L}{R_1}\right) + \left(\frac{\lambda L}{\pi w_1^2}\right)^2 \frac{1}{L}}{\left(1 - \frac{L}{R_1}\right)^2 + \left(\frac{\lambda L}{\pi w_1^2}\right)^2} + \frac{1}{\frac{j\pi w_1^2}{\lambda}\left[\left(1 - \frac{L}{R}\right)^2 + \left(\frac{\lambda L}{\pi w_1^2}\right)^2\right]} \qquad (1.23)$$

Calculate ρ_{out} using L and ρ_o, then R_{out} and w_{out} are related to the real and imaginary parts of ρ_{out}. In this way a Gaussian beam can be propagated through free space. The formalism is readily extended to

accommodate optical elements such as lenses and mirrors as well. (See Ref. 1.3).

Let's now look at the waist only:

$$w_2^2 = w_1^2 \left[\left(1 - \frac{z}{R}\right)^2 + \left(\frac{\lambda L}{\pi w_1^2}\right)^2 \right] . \qquad (1.24)$$

At the waist of a converging beam $R = \infty$ and $\frac{w_2}{w_1}$ attains a minimum.

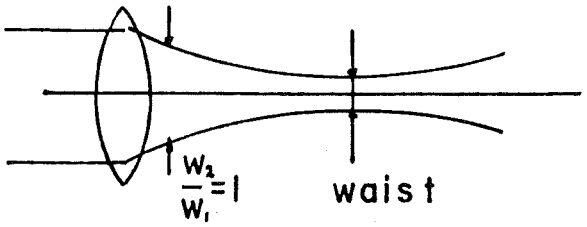


Figure I.6 Converging Gaussian beam.

Thus

$$\left(\frac{w_2}{w_1}\right)^2 = \left(\frac{\lambda L}{\pi w_1^2}\right)^2$$

or

$$\frac{w_2}{w_1} = \frac{\lambda L}{\pi w_1^2}$$

$$w_2 = \frac{\lambda L}{\pi w_1} \simeq \frac{\text{wavelength}}{\text{aperture}} = \text{distance} \qquad (1.25)$$

This result shows that the waist is determined by diffraction. The quantity $\frac{\text{wavelength}}{\text{aperture}}$ is the diffraction angle for an aperture of size w, and $\frac{\lambda L}{\pi w_1}$ is the displacement of the diffracted light in the

focal plane. The calculation of the waist diameter and the depth of focus can be easily performed using equations 1.23 and the results are given in appendix A.

1.3 Detectors:

A square law detector can be described by the following model:

$$\overline{i_p} = e_p^2(t) * g(t) \tag{1.26}$$

where

i_p is the detector output current

ℓ_p is the input electric field

$g(t)$ the transfer function of the detector

and

$$\overline{i_p} = \int_{-\infty}^{\infty} e_p^2(t') \left[\alpha\, e^{-\alpha(t-t')}\, u(t-t')\right] dt' \tag{1.27}$$

$$= e_p^2(t) * g(t)$$

$$g(t) = \alpha\, e^{-\alpha t}\, u(t)$$

$$u(t) = 0 \quad t \leq 0$$

$$= 1 \quad t > 0$$

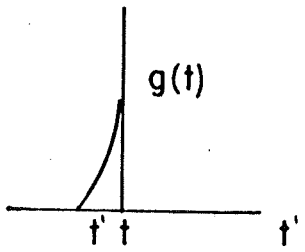


Figure I.7
Detector transfer function

The constant α determines the integration time or time constant of the detection system.

$\alpha \ll 1$ implies a large integration time.

$\alpha \gg 1$ implies a short integration time.

The integration time is of particular importance in interference phenomena.

1.4 Interferometry

Suppose we have an almost monochromatic light source with two closely spaced frequencies, ν_1 and ν_2 and we want to interfere the two beams in an interference experiment:

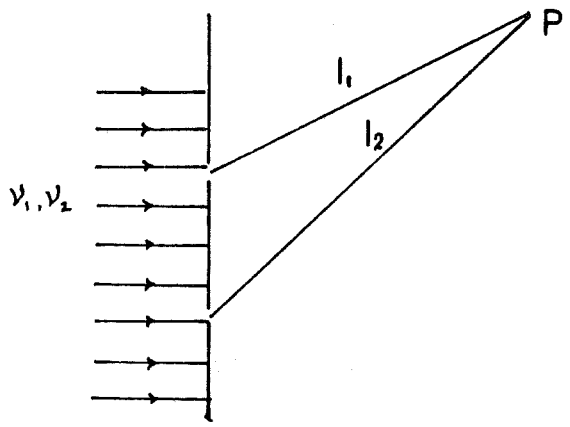


Figure I.8 Interference experiment

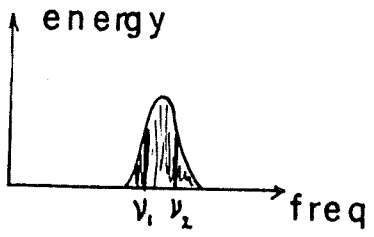


Figure I.9 Energy distribution of the light source.



Figure I.10 Time series of source energy.

The signal is periodic but not quite a sine wave and has a frequency distribution as depicted in figure

Suppose we deal with a real valued signal:

$$e(t) = e(\nu_1, t) + e(\nu_2, t) \tag{1.28}$$

Let

$$e_1 = e_{11}\left(\nu_1, t - \frac{\ell_1}{c}\right) + e_{12}\left(\nu_2, t - \frac{\ell_1}{c}\right)$$

$$e_2 = e_{12}\left(\nu_1, t - \frac{\ell_2}{c}\right) + e_{22}\left(\nu_2, t - \frac{\ell_2}{c}\right)$$

$$e_p = e_{11} + e_{12} + e_{21} + e_{22}$$

The intensity of the fringes is now given by

$$i_p = e_p^2(t) = (e_{11} + e_{12} + e_{21} + e_{22})^2$$

$$= e_{11}^2 + e_{12}^2 + 2e_{11}e_{12} + e_{21}^2 + e_{22}^2 + 2e_{21}e_{22} + 2(e_{11} + e_{12})(e_{21} + e_{22}) \tag{1.29}$$

Let

$$\begin{aligned} e_{11} &= \sin \nu_1 \left(t - \frac{\ell_1}{c}\right) \\ e_{12} &= \sin \nu_1 \left(t - \frac{\ell_2}{c}\right) \\ e_{21} &= \sin \nu_2 \left(t - \frac{\ell_1}{c}\right) \\ e_{22} &= \sin \nu_2 \left(t - \frac{\ell_2}{c}\right) \end{aligned} \tag{1.30}$$

Substitute (1.30) into (1.29) and take a <u>short</u> time average:

$$\begin{aligned} \overline{e_p^2}(t) = {} & 2 + \cos 2\pi \nu_1 \left(\frac{\ell_2 - \ell_1}{c}\right) + \cos 2\pi \nu_2 \left(\frac{\ell_2 - \ell_1}{c}\right) \\ & + \cos 2\pi (\nu_1 - \nu_2)\left(t - \frac{\ell_1}{c}\right) + \cos 2\pi (\nu_1 - \nu_2)\left(t - \frac{\ell_2}{c}\right) \\ & + \cos 2\pi \left[(\nu_1 - \nu_2)\, t + \frac{-\nu_1 \ell_1 + \nu_2 \ell_2}{c}\right] \\ & + \cos 2\pi \left[(\nu_1 - \nu_2)\, t + \frac{\nu_2 \ell_1 - \nu_1 \ell_2}{c}\right] \end{aligned} \tag{1.31}$$

For a long time average we get:

$$e_p^2(t) = 2 = 2\cos\left[\left(\frac{\nu_2 - \nu_1}{2}\right)\left(\frac{\ell_2 - \ell_1}{c}\right)\right]\cos\left[2\pi\left(\frac{\nu_1 + \nu_2}{2}\right)\left(\frac{\ell_2 - \ell_1}{c}\right)\right] \qquad (1.32)$$

The time average is called long if:

$$\frac{1}{\nu_1}, \frac{1}{\nu_2} \ll \tau \leq \frac{1}{\Delta\nu}$$

and short if:

$$\tau_{long} \gg \frac{1}{\Delta\nu}$$

For an argon-ion laser $\nu_1 - \nu_2 \approx 100$ mHz and $\tau_{long} \gg 10^{-8}$ sec. Therefore, photographic recordings are almost always long term averages. Note that the interference pattern (1.32) is slowly modulated by the term which depends on the difference frequency $(\nu_2 - \nu_1)$, while the high frequency fringe pattern is determined by the $\frac{\nu_2 + \nu_1}{2}$ term.

1.5 Index of Refraction

The index of refraction of a material determines the propagation speed of electro magnetic waves in that medium. A detailed derivation of this quantity is beyond the scope of this workshop but good accounts are given in Feynman (Ref. 1.5), Born and Wolf (Ref. 1.6) and Merzkirch (Ref. 1.7). Some of the physical concepts will be explained in this section and the relationship between the index of refraction and the density of a gas is derived.

Suppose a plane monochromatic wave is incident upon a material (such as glass) with an index of refraction $n \neq 1$, as shown in Figure I.. 11.

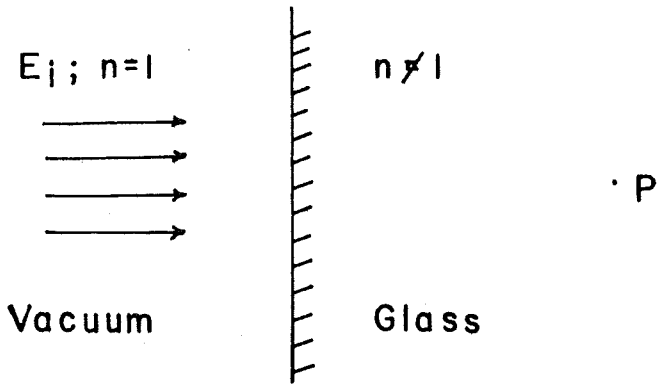


Figure I. 11. Plane wave incident upon glass plate.

At point P the electric field is given by

$$E_p = E_i + \sum_{\text{all other charges}} E_{\text{each charge}} \qquad (1.33)$$

In the glass the electrons are excited by the incoming harmonic wave and the moving charges generate a field which is given by the second term in equation (1.33). The motion of the electrons can be described by considering the equations for a damped harmonic oscillator.

$$F = q_e E = m(\ddot{x} + \gamma \dot{x} + \omega_o^2 x) \qquad (1.34)$$

where x is the displacement parallel to the direction of E, γ is the damping coefficient, ω_o is the resonance frequency and q_e denotes the charge of the electron.

Suppose $E = E_o e^{j\omega t}$

and therefore $x = x_o e^{j\omega t}$ (1.35)

Now substitute (1.35) in (1.34) and solve for x

$$x = \frac{q_e/m}{-\omega^2 + j\gamma\omega + \omega_o^2} \tag{1.36}$$

The index of refraction can now be calculated by introducing the induced dipole moment of an atom, which is equal to $q_e x$

or $$\vec{P} = \frac{q_e^2/m}{-\omega^2 + j\gamma\omega + \omega_o^2}\ \vec{E} \tag{1.37}$$

and $$\vec{P} = \epsilon_o \alpha(\omega) \vec{E} \tag{1.38}$$

can be expressed in terms of α the atomic polarizability.

where $$\alpha = \frac{q_e^2/m\epsilon_o}{-\omega^2 + j\gamma\omega + \omega_o^2} \tag{1.39}$$

If N is the number of atoms per unit volume in the material, then

$$\vec{P} = \epsilon_o N \alpha(\omega)\ \vec{E} \tag{1.40}$$

In nature, atomic systems can have several natural frequencies, indicated by ω_k, damping constants γ_k and the different modes have different strengths; this can be incorporated by multiplying the polarizability for each frequency by a factor f_x

Equation (1.39) can then be written as a sum.

$$\alpha(\omega) = \frac{q_e^2}{\epsilon_0 m} \sum_k \frac{f_x}{-\omega^2 + j\gamma_k\omega + \omega_0{}^2 k} \tag{1.41}$$

To obtain the electric fields the polarization is related to the charge density and the current density in the material and Maxwell's equations are solved by looking for wave like solutions.

The charge density is $\rho_{pol} = -\nabla\cdot\vec{P}$ (1.42)

and the current density is $j_{pol} = \frac{d\vec{P}}{dt}$

Upon substitution of (1.42) and (1.43) in Maxwell's equations and after some algebra we find:

$$\nabla^2 E - \frac{1}{c^2}\frac{\partial^2 E}{\partial t^2} = -\frac{1}{\epsilon_0}\nabla(\nabla\cdot\vec{P}) + \frac{1}{\epsilon_0 c^2}\frac{\partial^2\vec{P}}{\partial t^2} \tag{1.44}$$

Assume now that $\vec{P}$ is in the same direction as $\vec{E}$ (isotropic materials) and let E be polarized in the x direction

$$\begin{aligned} E_x &= E_o\, e^{j(\omega t - kz)} \\ &= E_o\, e^{-jk(z - \frac{\omega}{k}t)} \\ &= E_o\, e^{j(\omega t - \omega nz/c)} \end{aligned} \tag{1.45}$$

because the phase velocity is given by $v_{ph} = \frac{\omega}{k} = \frac{c}{n}$ where n is the index of refraction. (1.46)

For an isotropic material $\vec{P} = P_x$ and assume $P_x \sim e^{j\omega t}$ then eqn. (1.44) reduces to

$$-k^2 E_x + \frac{\omega^2}{c^2} E_x = -\frac{\omega^2}{\epsilon_o c^2} P_x \tag{1.47}$$

use $P_x = \epsilon_o N\alpha E_x$ and (1.47) becomes

$$k^2 = \frac{\omega^2}{c^2}(1 + N\alpha) \tag{1.48}$$

Now (1.46) and (1.48) imply: $n^2 = 1 + N\alpha$ or using (1.39)

$$n^2 = 1 + \frac{Nq_e^2}{m\epsilon_o} \frac{1}{-\omega^2 + i\gamma\omega + \omega_o^2} \tag{1.49}$$

or using (1.41)

$$n^2 = 1 + \frac{Nq_e^2}{m\epsilon_o} \sum_k \frac{f_x}{-\omega^2 + i\gamma k\omega + \omega_o^2 k} \tag{1.50}$$

For gases $n^2 - 1 = k\rho$, which is referred to in the literature as the Gladstone-Dale law where ρ is the density of the gas and k the Gladstone-Dale constant. k can be calculated from (1.50) and (1.51) and realizing that N, M and ρ are related. The density ρ is given by:

$$\rho = \frac{NM}{\mathcal{L}},$$

where M is the molecular weight and $\mathcal{L}$ Loschmidt's number (the number of molecules per unit volume of an ideal gas at 0° C and at

normal atmospheric pressure $\mathcal{L} = (2.68719 \pm .0001) \times 10^{19}$ cm^{-3}).

For an ideal gas the pressure, density and temperature are related by $p = \rho R T$ where R is the gas constant and T the absolute temperature.

Equations (1.50) and (1.51) can now be used to compute a thermodynamic quantity, such as P, T or the density in terms of the index of refraction (eqns. 1.50, 1.51). For most gases at atmospheric pressure and temperature, k is a constant and n is therefore directly related to ρ.

A plot of n versus frequency shows an interesting behavior.

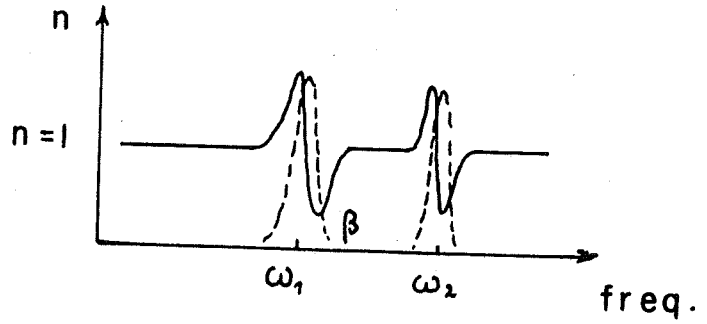


Figure Index of refraction and absorption coef. β as a function of frequency.

Near the resonance frequencies the index of refraction can attain values many orders of magnitude greater than in the non-resonant case, and the absorption coefficient attains a maximum at resonance as well. The relationship between the absorption coefficient and the index of refraction can be obtained writing n as a complex quantity:

$$n = n_r - i n_I$$

and $$E_x = E_0 e^{-j\omega (t - n z/c)}$$

or $E_x = E_o\, e^{-\omega n_I z/c}\, e^{j\omega(t - n_R z/c)}$

This shows that the amplitude of the wave decreases exponentially with z, or the intensity goes like

$$\text{Intensity} \sim e^{-2\omega n_I z/c} \equiv e^{-\beta z}$$

where $\beta = 2\omega n_I/c$ represents the absorption coefficient. Thus, the theory of index of refraction and absorption are closely related.

Experimentally the large change in index of refraction near resonance can be successfully used to visualize gas flows at low pressure or acoustic waves of small amplitude. This application will be treated in Section II.

Section II Modern Interpretation of Classical Instruments and Image Processing

2.1 Optical Processor.

The optical processor configuration, as shown in Figure (2.1) forms the basis for understanding modern optical processors and the schlieren system. The system consists of two double convex lenses which image a point light source from the focal plane of the first lens onto the back focal plane of the second one, which can be referred to as the optical Fourier transform (OFT) plane (cf. Fig. 2.1), and a third lens which images the object onto the film. For the purpose of describing the system, without sacrificing the essential physics in the problem the discussion will be restricted here to monochromatic sources. In principle, the results can be extended to polychromatic radiation, but the mathematics describing the setup becomes considerably more involved.

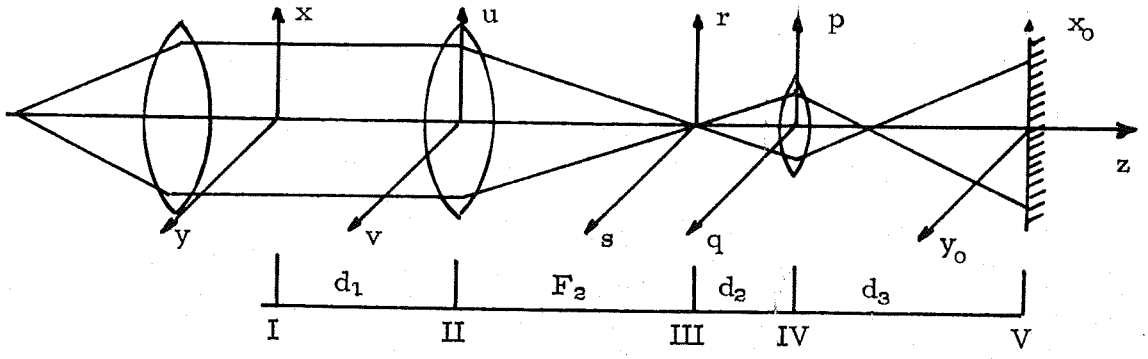


Figure 2.1 Schematic of an Optical Processor

Consider the geometry of Figure 2.1 with a rectangular coordinate system (x, y), (u, v), (r, s) and (p, q) attached to the planes I, II, III, and IV, resepctively. The object, located a distance d_1 in front of the lens, is illuminated by a normally incident plane wave of unit amplitude. The transmittance of the object is denoted by $E_I(x, y)$, where the harmonic phase factor $e^{-j\omega t}$ is omitted. In

plane III, the electric field amplitude can be computed using diffraction theory and is given by

$$E_{III}(r,s) = \frac{1}{j\lambda F_2} \exp\left\{ j \frac{k}{2F_2} \left(1 - \frac{d_1}{F_2}\right)(r^2 + s^2)\right\}$$
$$\iint_{-\infty}^{\infty} E_I(x,y)\, P\left(x + \frac{d_1}{F_2} r,\ y + \frac{d_1}{F_2} s\right) \exp\left[-j \frac{k}{F_2}(xr + ys)\right] dxdy \tag{2.1}$$

where P is the pupil function for lens 2, i.e.,
$P\left(|x| > D_2/2,\ |y| > D_2/2\right) = 0$ and $P\left(|x| \le D_2/2,\ |y| \le D_2/2\right) = 1$
Applying this same formula again to propagate the field distribution from plane III to plane V, $E_V(x_o, y_o)$ is found to be

$$E_V(x_o, y_o) = \exp\left\{ j \frac{k}{2F_3} \left(1 - \frac{d_2}{F_3}\right)\left(x_o^2 + y_o^2\right)\right\}$$
$$\iint_{-\infty}^{\infty} E_{III}(r,s)\, P\left(r + \frac{d_2}{F_3} x_o,\ s + \frac{d_2}{F_3} y_o\right) \tag{2.2}$$
$$\exp\left\{ - j \frac{k}{F_3}(r x_o + s y_o)\right\} dr\, ds$$

where again P is the pupil function for lens 3. In addition, if the camera focuses onto the object plane, then d_1, d_2, d_3, F_2 and F_3 are related by using the lens law:

$$d_3 = \frac{\left(d_2^2 - F_2^2 - d_1 F_2\right) F_3}{F_3 F_2 - F_3 d_2 - d_2^2 - F_2^2 - d_1 F_2} \tag{2.3}$$

Combining equations 2-1, 2-2 and 2-3, $E_V(x_o, y_o)$ can be expressed in terms of $E_I(x,y)$ and geometrical parameters. The result of this calculation is not of immediate interest here, but will be presented for the OFT plane photography in Section 2.3, while in

2.2, 2.3, 2.4, and 2.5 the above discussion will be used as a starting point for the treatment of the modifications of this basic scheme.

2.2 Schlieren System

The schlieren system is identical to that of the optical processor described in Section 2.1, except that the frequency content of the signal in the OFT plane is altered. This is accomplished by inserting a knife blade into the focal spot or by blocking the low frequencies with a dot. A knife blade with the cutting edge oriented parallel to the s coordinate and passing through the origin changes the limits of integration in equation 2.2 to the following:

$$E_V(x_o, y_o) = \exp\left\{\frac{jk}{2F_3}\left(1 - \frac{d_2}{F_3}\right)\left(x_o^2 + y_o^2\right)\right\}\int_0^{\infty}\int_{-\infty}^{\infty} E_{III}(r, s)$$
$$P\left(r + \frac{d_2}{F_3}x_o,\ s + \frac{d_2}{F_3}y_o\right)\exp\left[-j\frac{k}{F_3}(rx_o + sy_o)\right]dr\,ds \qquad (2.4)$$

A dot with radius R centered around the origin modifies equation 2.2 to

$$E_V(x_o, y_o) = \exp\left\{\frac{jk}{2F_3}\left(1 - \frac{d_2}{F_3}\right)\left(x_o^2 + y_o^2\right)\right\}\int_R^{\infty}\int_R^{\infty} E_{III}(r, s)$$
$$P\left(r + \frac{d_2}{F_3}x_o,\ s + \frac{d_2}{F_3}y_o\right)\exp\left[-j\frac{k}{F_3}(rx_o + sy_o)\right]dr\,ds$$

where $r^2 + s^2 \geq R^2$

Equations 2.1 and 2.3 are not altered as long as it is kept in mind that euqation 2.1 is valid an infinitesimal distance upstream of the stops. Just behind these obstructions equation 2.1 is only applicable

for either $r > 0$, in case of the knife blade, or $r^2 + s^2 > R^2$ for the dot with radius R.

Recently Bershader (Ref. 2.1) has proposed to use the resonant refractive behavior of sodium to visualize weak sound waves or other density disturbances which cannot readily be seen with a conventional schlieren system. In this system sodium vapor is introduced in the test section and a tunable dye laser is used to excite the molecules near the resonance condition. As a light source for the schlieren system a sodium vapour lamp should be used. It is theoretically estimated that soundwaves as weak as 82 dB can be observed.

2.3 Shadowgraph System

This method records the shadows cast by the object onto a photographic plate. The camera and second lens are replaced by a single photographic plate holder. The equations, 2.1 - 2.3, do not describe this system adequately. This configuration, however, has been analyzed in some detail by Taylor (Ref. 2.2), for the case of light propagating through turbulence. The schlieren setup can be easily modified into a shadowgraph system by inserting a film plate holder between the object and the second lens.

2.4 Optical Correlator

Shadowgraph and schlieren pictures can be used to obtain space-correlation functions as first described by Uberoi and Kovasznay (Ref. 2.3). The method consists of making two identical transparencies of the original negative. The two copies are then placed back to face in an optical processor between the first two lenses. A photo detector is substituted for the camera and is

located in the OFT plane. The two transparencies are matched and the transmitted intensity is measured as a function of the displacement away from this position. Using the assumption of homogeneous and isotropic turbulence, the correlation function of the three-dimensional density field can be recovered.

The analysis for correlation functions obtained from schlieren pictures is given by Thompson and Taylor (Ref. 2.4), using ray optics.

Uberoi and Kovasznay (Ref. 2.3) first proposed the technique for obtaining three-dimensional space-correlation functions of a density field using two-dimensional space-correlation functions acquired from shadowgraph pictures. Their method principally relies on the assumption of a statistically homogeneous and isotropic flow. First, the correlation function measured in the optical correlator has to be provided with an ordinate. The peak in the curve corresponds to perfect alignment of the two transparencies and is denoted by 1, the normalized correlation coefficient. The position of the origin, which signifies zero correlation, cannot be directly measured. However, it can be shown that the first and third moments of the correlation function have to be zero for isotropic turbulence, if the light path through the medium is long compared with the integral scale

$$\int_0^\infty \beta(\xi)\, \xi \, d\xi = \int_0^\infty \beta(\xi)\, \xi^3 \, d\xi = 0 \qquad (2.6)$$

where $\beta(\xi)$ is the measured picture correlation function. The correlation function for the flow can then be computed according to

$$R(r) = \frac{1}{8\pi D}\left(\frac{\rho_o}{kd}\right)\int_r^\infty \beta(y)\left[y\frac{2r^2 + y^2}{r}\cos^{-1}\left|\frac{r}{y}\right| - 3y\,(y^2 - r^2)^{\frac{1}{2}}\right]dy$$

where ρ_o signifies the mean density, D denotes the thickness of the slab of turbulence, k is a constant associated with the photographic process, d is the distance between the density field and the photographic plate, and r is the displacement over which the correlation function is computed. In many cases though, the sole purpose of the correlation function is the determination of scales of turbulence. (Hesselink, Ref. 2.5) For that purpose equation (2.7) does not have to be computed. The integral scale L_ρ and the microscale, λ_ρ can be expressed immediately in terms of $\beta(r)$ from equation (2.7).

$$L_\rho = \int_o^\infty \frac{R(r)\,dr}{R(o)} = \frac{-\frac{\pi}{8}\int_o^\infty \beta(\xi)\,\xi^3 \log \xi\, d\xi}{\int_o^\infty \beta(\xi)\,\xi^2\, d\xi} \qquad (2.8)$$

$$\lambda_\rho^2 = -2\,R(o)\,R''(o) = \frac{-6\int_o^\infty \beta(\xi)\,\xi^2\, d\xi}{\int_o^\infty \beta(\xi)\, d\xi} \qquad (2.9)$$

From the equation 2.8 it can be seen that L_ρ depends principally on the behavior of $\beta(\xi)$ for large values of ξ; however, the correlation function is the least accurate there, mainly because the shadowgraph technique de-emphasizes the low wave number contribution that determines L_ρ. Therefore, it is to be expected that, using this method, the microscale is more accurately determined than the integral scale. A major difficulty arises with this method when the density gradients become strong enough to form foci or caustic surfaces within the scattering region.

A novel way of obtaining turbulent scales to avoid this problem is described in Section III. The wave length dependence of speckle can be used to obtain the correlation function of the medium. This technique involves the use of an imaged speckle pattern and therefore is superior to the shadowgraph method.

2.5 Calculation of a Length Scale for a Density Field Using Optical Fourier Transform Photography

To study turbulence (Hesselink, Ref.2.6) one can very effectively look at the spot in the back focal plane of the second lens and determine a length scale of the scattering medium. This system is explained here.

The equations, which are presented in Section 2.1 to describe the properties of the optical processor, are based on diffraction theory. Using equation 2.1 as a starting point, the effective radius of the focal spot in a system with a slab of turbulence present between the two lenses can be computed. This calculation, which is valid for square aperture pupil functions, is lengthy. However,

the wavelength of light is small compared with the smallest scale in the turbulence, $\lambda << \lambda_\rho$, and also $\lambda D << \lambda_\rho$, where D is the thickness of the slab. Therefore, geometrical optics can be used as a valid approximation to diffraction theory. The calculation then becomes relatively simple and will be presented here.

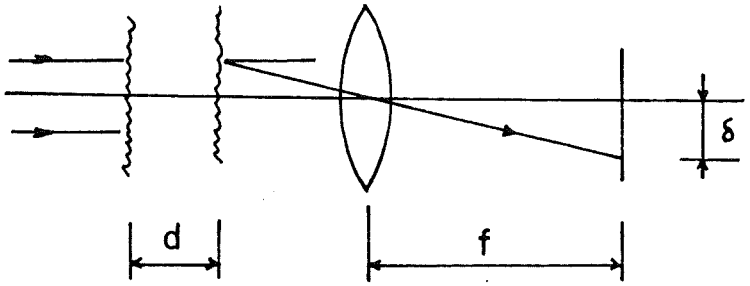


Figure 3.2 Optical Setup for Fourier Transform Photography

Consider the optical arrangement of figure 3.2. The scattering medium is characterized by a fluctuating index of refraction $n = 1 + \mu$, where $\mu << 1$, and a space-correlation function N. The mean angle of deviation of a ray from its initial direction is denoted by $\bar{\theta}$.

$$\bar{\theta} = 4K_1 D \tag{2.10}$$

where K_1 is a constant (Chernov, Ref.2.7). In the case of isotropic scattering K_1 takes on the value

$$K_1 = -\tfrac{1}{2}\overline{\mu^2} \int_0^\infty \frac{1}{2}\frac{\partial}{\partial_r}\left(r^2 \frac{\partial N}{\partial r}\right) dr \ . \tag{2.11}$$

The mean radius of the focal spot in the presence of turbulence, R_{turb}, can now be computed simply using

$$\overline{\delta} = \overline{\theta} \cdot F \ . \qquad (2.12)$$

Thus, by measuring $\overline{\delta} = R_{turb} - R_{noturb}$, the effect of the scattering medium on the impulse response of the system can be evaluated. The scale L_ρ can be computed from equations 2.10, 2.11 and 2.12 using an assumed shape for the correlation function N.

Image Processing

An example of an analog image processing system is the optical correlator and others will be given in class. An example of a digital image processing is also treated in class.

References

1. 1 Goodman, J.W. 1968 Introduction to Fourier Optics. McGraw-Hill, New York.

1. 2 Lengyel, B.A. 1971 Lasers. Wiley-Interscience, New York.

1. 3 Siegman, A.E. 1968 An Introduction to Lasers and Masers. McGraw-Hill, New York.

1. 4 Yariv, A. 1975 Quantum Electronics. John Wiley and Sons, New York.

2. 1 Bershader, D. et al 1977 Improved flow visualization by use of resonant refractivity. Experimental Diagnostics in Gas Phase Combustion Systems. Vol. 53, Progress in Astronautics and Aeronautics. AIAA, New York.

2. 2 Taylor, L.S. 1969 AIAA Journal 8, p. 1284.

2. 3 Uberoi, M.S. and Kovasznay, L.S.G. 1954 Journal of Applied Physics 26, p. 19.

2. 4 Thompson, L.L. and Taylor, L.S. 1969 AIAA Journal 7, p. 2030.

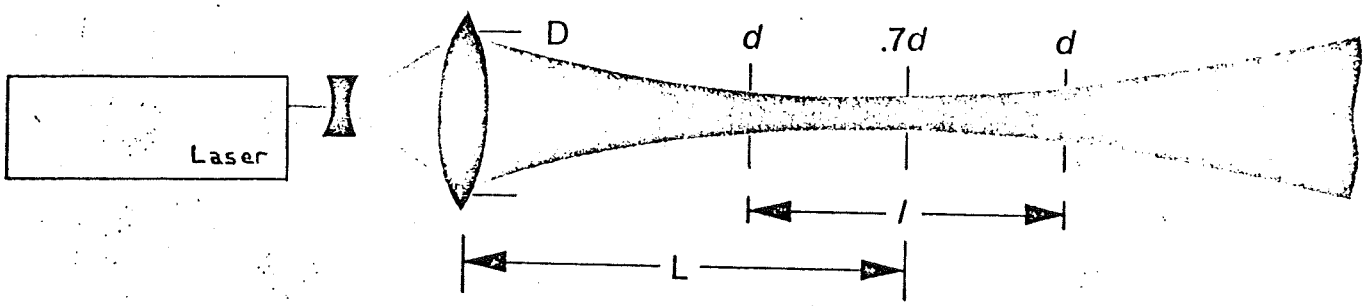
2. 5 Hesselink, L. 1977 An Experimental Investigation of the Propagation of Weak Shock Waves through a Random Medium. Proceedings of the Eleventh International Symposium on Shock Tubes and Waves. Seattle, 11 - 14 July 1977.

2. 6 Hesselink, L. 1977 An Experimental Investigation of the Propagation of Weak Shock Waves Through a Random Medium. Ph.D. Thesis, California Institute of Technology.

2. 7 Chernov, L.A. 1960 Wave Propagation in a Random Medium. McGraw-Hill, New York.

Laser depth of field:

How small a spot can be maintained for how great a distance?



d = beam diameter
l = length or "depth of field" within which the beam is less than d
D = beam diameter at collimator exit
L = length from collimator to midpoint of depth of field

Depth of field

F F number	l Depth of field (inches)	d Beam diameter (inches)
20	0.026	0.0009
50	0.16	0.0023
100	0.64	0.0045
200	2.56	0.009
250	4.0	0.011
300	5.8	0.014
400	10.2	0.018
500	16	0.023
1000	64	0.05
2500	400	0.11
5000	1600	0.23

Where F is the F number of the collimating optics, theoretical calculations for 633 nm helium-neon laser light can be based on the values:

$l = 6.4 \times 10^{-5} F^2$ inches or $1.63 \times 10^{-3} F^2$ mm
$d = 4.5 \times 10^{-5} F$ inches or $1.14 \times 10^{-3} F$ mm

These theoretical limits may not be attained in practice, but a variance of less than 10% can be attained with care.

Where L and D are given in the same units of measurement, F can be approximated using the formula:

$$F = \frac{L}{D}$$

"I need a 1 mm spot for a 1 meter distance. Is it possible? What telescope do I use?"

Judging by the number of calls we receive, the depth of field of laser light deserves some explanation.

Depth of field is the distance over which the diameter of the beam never exceeds a given value.

With laser light the answers to depth of field questions are straightforward: as the spot size becomes wider, the depth of field becomes longer. Beam diameter and depth of field are dependent. One value or the other may be chosen, but not both.

To answer your depth of field questions, we offer the table and the formulas at the left.

To solve your depth of field problems, we offer four new collimators listed below.

60-260	3x magnification; F ≃ 5 to infinity. $40.00
60-265	6x magnification; F ≃ 47 to infinity; contains 35 micron spatial filter. $85.00
60-270	13x magnification; F ≃ 39 to infinity. $50.00
60-275	20x magnification; F ≃ 38 to infinity. $60.00

Each of the collimators is a focusing telescope. On the 6x, 13x, and 20x models, the important objective lens is a high quality corrected doublet. Use the reader response number to receive full specifications.

143 HARDING AVENUE, BELLMAWR, NEW JERSEY 08030
609-933-0100 • CABLE: METROLOGIC • TELEX: 83-4694

Metrologic

HOLOGRAPHY

8.1 Introduction:

Holography was invented by Denis Gabor in 1948 for the purpose of improving the performance of electron microscopes. In recognition for this work he received the Nobel Prize. The term holography is derived from the Greek words holos, which means entire and gramma which means writing or that which is written. Therefore, the name suggests the underlying feature of holography, namely that in one way or another everything is known about the object field. That is to say, both the phase and amplitude of the wavefield can be retrieved from stored intensity information. In optics one is hampered by the very high frequencies of the electro magnetic waves and at present no detectors exists which are capable of measuring both the phase and amplitude of an optical wavefield. In other branches of physics, for instance in acoustics, one can in fact measure both the amplitude and phase of acoustic waves, but no equivalent of the photographic plate exists. Gabor, in his ingeneous way, combined knowledge of several areas of optics, in particular diffraction and partial coherence theory and devised a method by which information about an object wave can be stored on a photographic plate or some other recording material and this information can later be retrieved by a suitable readout method.

The method of holography basically consists of the following steps. First the object wave, for instance the scattered radiation coming from a solid object is incident upon a photographic plate. Simultaneously a reference wave of the same frequency is also incident on the plate and the two beams produce an interference pattern. That intensity pattern is recorded on the film and after development the developed plate, which is commonly called the hologram, is illuminated by a reconstruction wave. Quite often the reconstruction wave is identical to the reference wave, but it need not be. Certain holograms, called white-light holograms, can be read out using ordinary incandescent light bulbs. During the recording process, however, it is needed that the object and reference wave are capable of producing a stationary fringe pattern, at least during the exposure time. The hologram acts like a diffraction grating and the object

wave is one of the diffracted wavefields that is generated by illumination with the reconstruction wave.

To understand this process in more detail, the basic steps in the holographic procedure will be analyzed.

a. Hologram Construction:

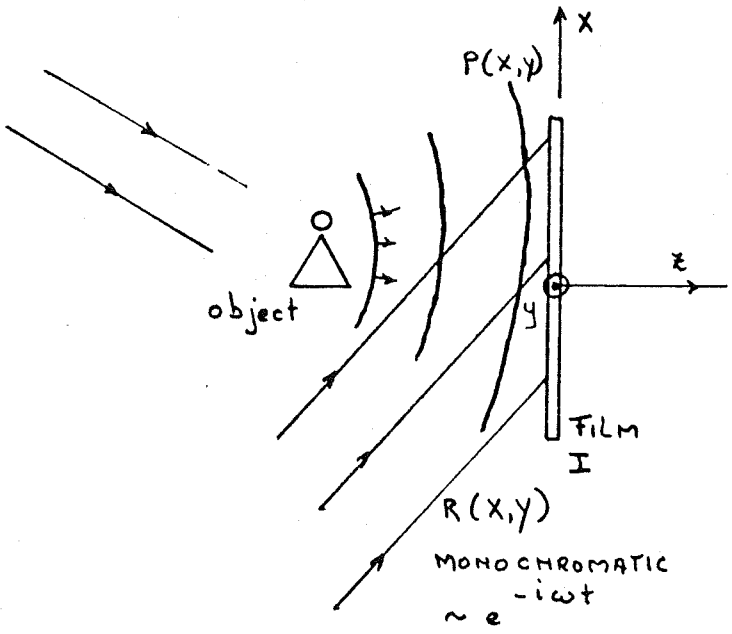


Figure 8.1 Hologram Construction Configuration

An object is illuminated by a coherent wave, such as a laser beam, and the scattered picture wave P(x,y) is incident upon the photographic plate. The plate is located in the x-y plane and a reference wave, indicated by R(x,y) is incident as well. In practice the reference wave is often taken to be a diverging spherical wave or a plane wave, however any wave that is capable of producing a fringe pattern with the object wave will do. Again we suppress the $e^{-i\omega t}$ time dependence in the analysis. The field at plane I is now given by:

$$F_I = P(x,y) + R(x,y)$$

and the intensity pattern is then:

$$I_I = F_I F_I^* = \left[P(x,y) + R(x,y) \right] \left[P(x,y) + R(x,y) \right]^*$$

$$\left[e^{-i\omega t} \quad e^{i\omega t} \right]$$

or

$$= PP^* + PR^* + RP^* + RR^*$$

$$\boxed{I_I = |P|^2 + |R|^2 + PR^* + RP^*} \qquad (8.1)$$

The object and reference wave produce a fringe pattern that is recorded on the film.

b. Development of the exposed film:

The physical process that take place in the development procedure can be satisfactorily modeled by the simple relation:

$$T_H = CI^{-\gamma/2} \qquad (8.2)$$

where T_H is the amplitude transmittance of the developed film, γ is a film constant and depends on the development procedure and C is a film and development related constant. The relation (8.2) is often called the Hurter-Driffield relationship when T_H is replaced by the density of the film, which is T_H = log ^{1}/transmittance.

Suppose now that the experimenter controls the development process such that $\gamma = -2$ and $C = 1$. Then the relationship (8.2) becomes very simple

$$T_H = I \qquad (8.3)$$

i.e., the hologram transmittance is directly equal to the intensity of the interference pattern in the recording process. Even if $C \neq 1$ and $\gamma \neq -2$ the holographic procedure works, except that the analysis becomes more cumbersome.

Thus:

$$T_H(x,y) = |R^2| + |P|^2 + PR^* + RP^* \qquad (8.4)$$

c. Illumination Of The Hologram With The Reference Wave:

The hologram is now illuminated with the reconstruction wave and for simplicity it is assumed that both the angle of incidence and the wave-front are kept the same as for the reference wave during the recording process.

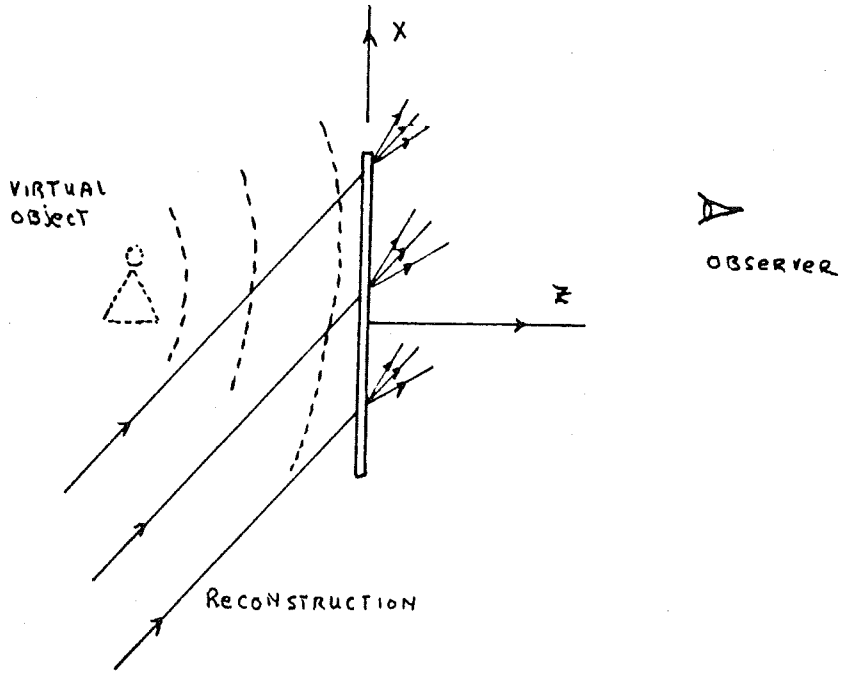


Figure 8.2 Object Reconstruction Configuration

Then the output field from the hologram is:

$$T_H R = |R|^2 R + |P^2|R + PR^* R + P^* RR$$

$$= \left\{ |R|^2 + |P|^2 \right\} R + |R|^2 P + P^* R^2 \qquad (8.5)$$

Physically the three terms on the right hand side of (8.5) can be interpreted as follows. The first term represents the transmitted reference wave. The direction is equal to the direction of the incoming wave, but the amplitude is modified by the term in brackets. The second term represents the picture wave. This wave has the same phase and direction as the original picture wave, but the amplitude is modified by the $|R|^2$ term. The last term is the conjugate picture wave. This wave travels in a different direction than the original picture wave and has a different amplitude as well. Thus, upon reconstruction three wave fields are generated, one of which is identical, except for intensity, to the original picure wave. The hologram evidently acts like a diffraction grating and produces two diffracted wave fields, one being the original picture wave and one the conjugate picure wave, besides the transmitted reconstruction wave. This point can be illustrated further by considering a reference wave and object wave that are described by:

$$R(x,y) = R_o\, e^{i\vec{k_r}\cdot\vec{r}}$$
$$P(x,y) = P_o\, e^{i\vec{k_p}\cdot\vec{r}} \qquad (8.6)$$

Thus according to (8.5) the reconstructed field is represented by:

$$T_H R = (R_o^2 + P_o^2)\, R_o\, e^{i\vec{k_r}\cdot\vec{r}} + R_o^2\, P_o\, e^{i\vec{k_p}\cdot\vec{r}} + P_o\, e^{-i\vec{k_p}\cdot\vec{r}}\, R_o^2 e^{i_2\vec{k_r}\cdot\vec{r}} \qquad (8.7)$$

It is instrutive to interpret this result. Suppose a point source is located at P and at point A on the film plate the object wave and reference wave have wave vectors that are denoted by $\vec{k_r}$ and $\vec{k_p}$ as drawn in Figure 8.3. The two waves are superimposed and form an interference pattern that is characterized by a grating vector, which is in the direction $\vec{k_g} = \vec{k_p} - \vec{k_r}$, and is perpendicular to the fringes. This relationship can be checked very easily by considering the super position of two plane waves. Thus everywhere in the hologram the fringes are characterized by a grating vector $\vec{k_g}$, which depends on the local object and reference wave vectors during the recording phase. Upon illumination of the hologram by a reconstruction wave in the $\vec{k_c}$ direction a diffracted wave is generated in the $\vec{k_d}$ directions:

For the picure wave: $\vec{k}_d = \vec{k}_c + \vec{k}_g = \vec{k}_c + \vec{k}_p - \vec{k}_r = \vec{k}_p + (\vec{k}_c - \vec{k}_r)$

For the conjugate wave: $\vec{k}_d = \vec{k}_c - \vec{k}_g = \vec{k}_c + \vec{k}_r - \vec{k}_p$ (8.8)

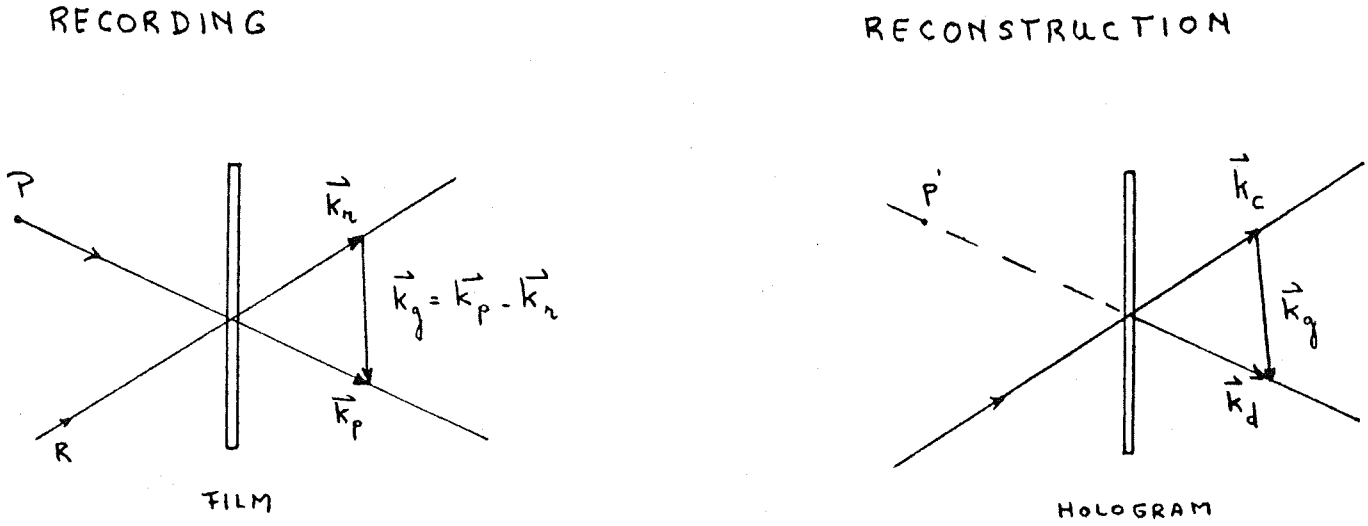


Figure 8.3 Recording and Reconstruction Wave Vectors

Where: $\vec{k}_r$ = reference wave vector

$\vec{k}_p$ = picture wave vector

$\vec{k}_c$ = reconstruction wave vector

$\vec{k}_d$ = diffracted wave vector

Equation (8.8) shows directly that if the hologram is illuminated by the reference wave $\vec{k}_d = \vec{k}_p$ for the picture wave and $\vec{k}_d = 2\,\vec{k}_r - \vec{k}_p$ for the conjugate wave. The latter wavefield is related to the object field but in general is highly distorted.

A simple example illustrates the point. Let a square be illuminated

by a laser beam and a reference plane wave is incident upon the film plate during the recording process at an angle $\alpha = 30^{\circ}$ with respect to the z-axis. The film plate is developed and the hologram is illuminated by a reconstruction plane wave in the same direction as the original reference wave, namely $\alpha = 30^{\circ}$. A few ray vectors are drawn in the diagram to show the reconstruction. Both the reconstructed square as well as the distorted conjugate wave are shown. For an observer to the right of the hologram, the original object appears behind the hologram and is virtual and the distorted conjugate picture is in front and real. By properly positioning the observer with respect to the hologram, only the virtual object can be seen and the distorted object is out of the field of view.

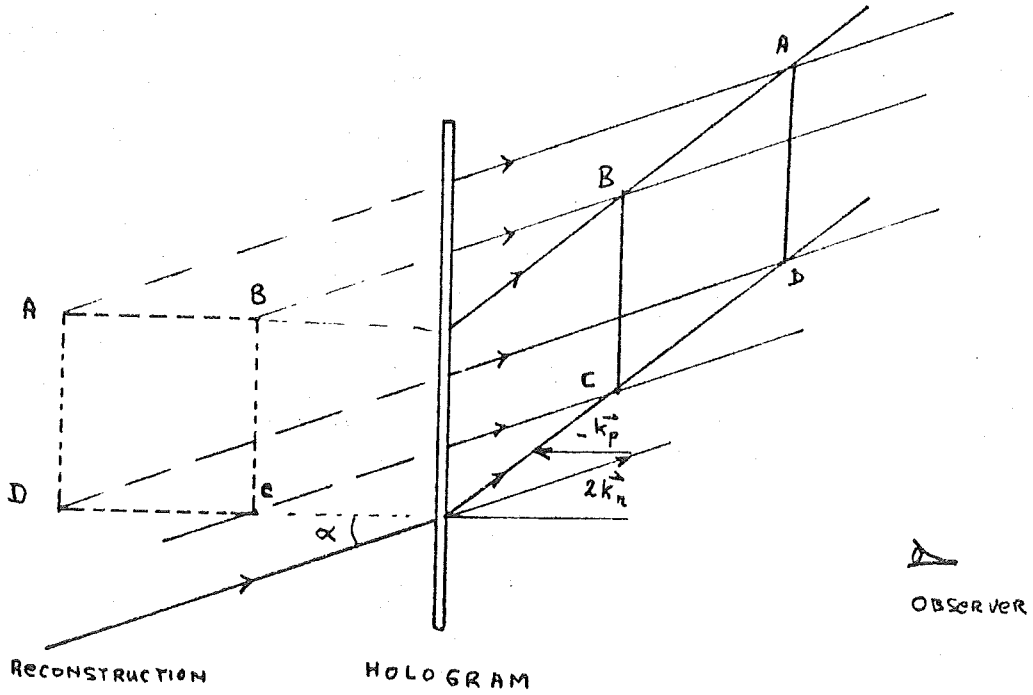


Figure 8.4 Real and Virtual Reconstructions of a Square

This aspect of the reconstruction process is due to Leith and Upatnieks, who first produced an off-axis hologram in the early 1960's, in which the two reconstructed images are separated from each other. Gabor originally made a so called in-line hologram as shown in Figure 8.5. In this set up the two images cannot be separated and are called twin images. Gabor was forced

to use this arrangement because he did not have a coherent light source available to him. This draw back of the method prevented holography from

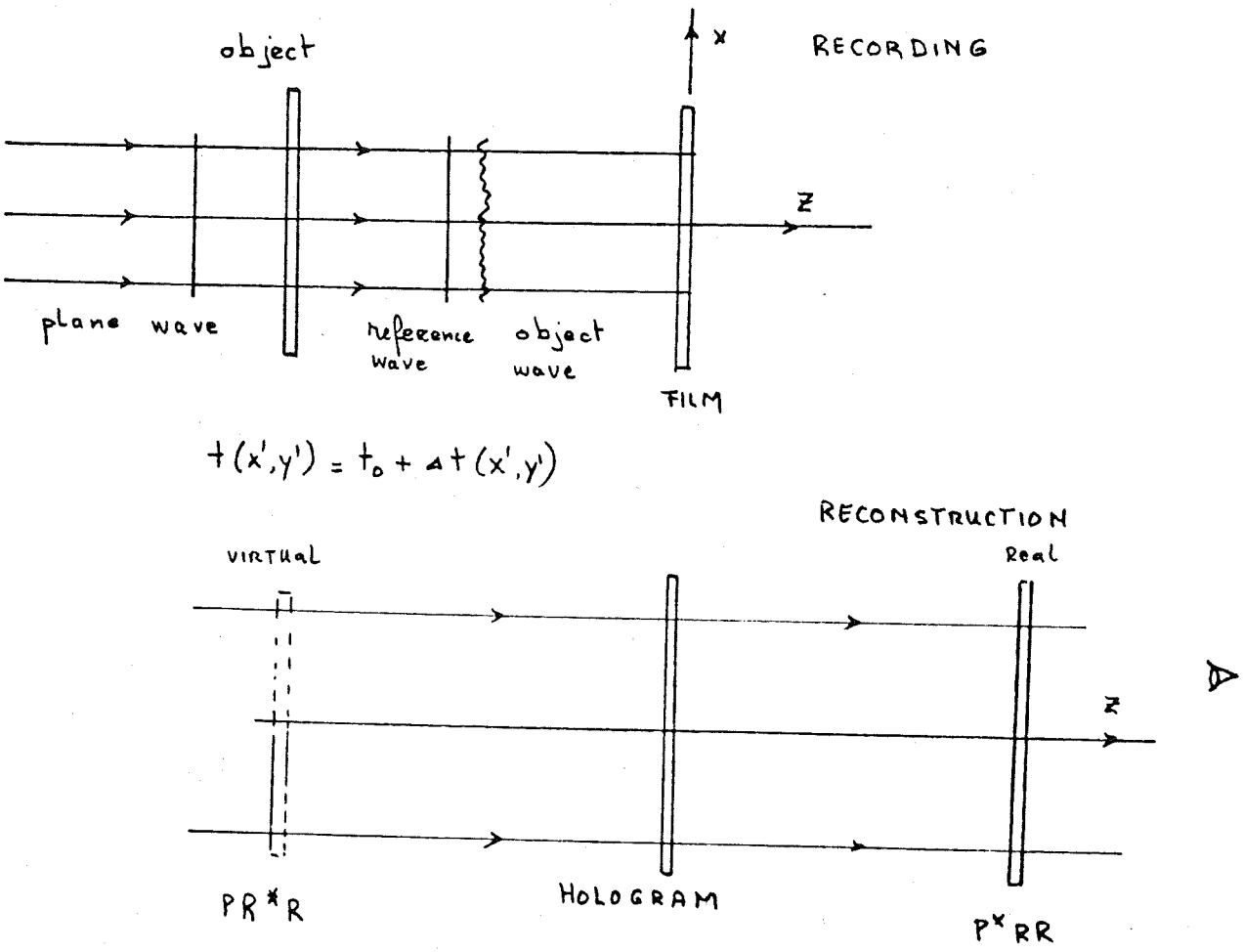


Figure 8.5 In-Line Hologram Configuration

becoming popular until the invention of the laser in 1960 and Leith and Upatnieks contribution to off-axis holography.

Finally it is interesting to explore other reconstruction techniques. The hologram can be illuminated by a wave that has the same phase front and intensity characteristics as the reference wave, but is instead propagating in the opposite direction. This reconstruction wave is called the conjugate reference wave and upon illumination of the hologram two wavefields are generated besides the undisturbed, except for amplitude, transmitted reconstruction wave. An observer located at the opposite side of the hologram, i.e., looking towards the reconstruction wave will see a real reconstructed image and a virtual distorted conjugate image as shown in Figure 8.6.

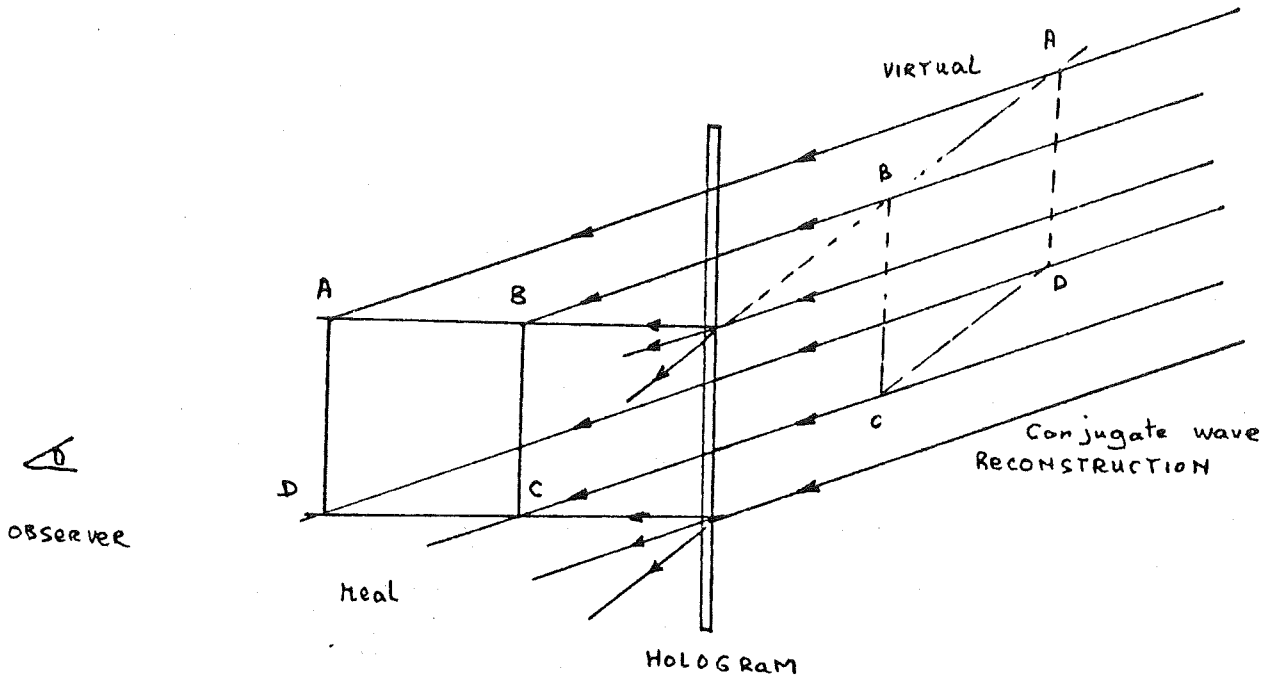


Figure 8.6 Conjugate Wave Reconstruction

Notice that to this observer the relative position from the four points ABCD of the square has been reversed compared with the perspective that an observer to the right of the square has, while viewing the object. In the conjugate beam reconstruction it is as if one looks at a transparent mask from behind. This image is often referred to as pseudo scopic for this reason.

Types Of Holograms:

Holograms can be distinguished on the basis of their diffraction properties into two broad classes, plane and volume holograms. A plane hologram acts like a thin diffraction grating which can be described by a two dimensional transmission function T_H (x,y) and a volume hologram satisfies the Bragg-refraction laws and is described by a three dimensional

transmission function $T_H(x,y,z)$. The type of hologram that results depends on the recording configuration. As an example consider the super position of two plane waves.

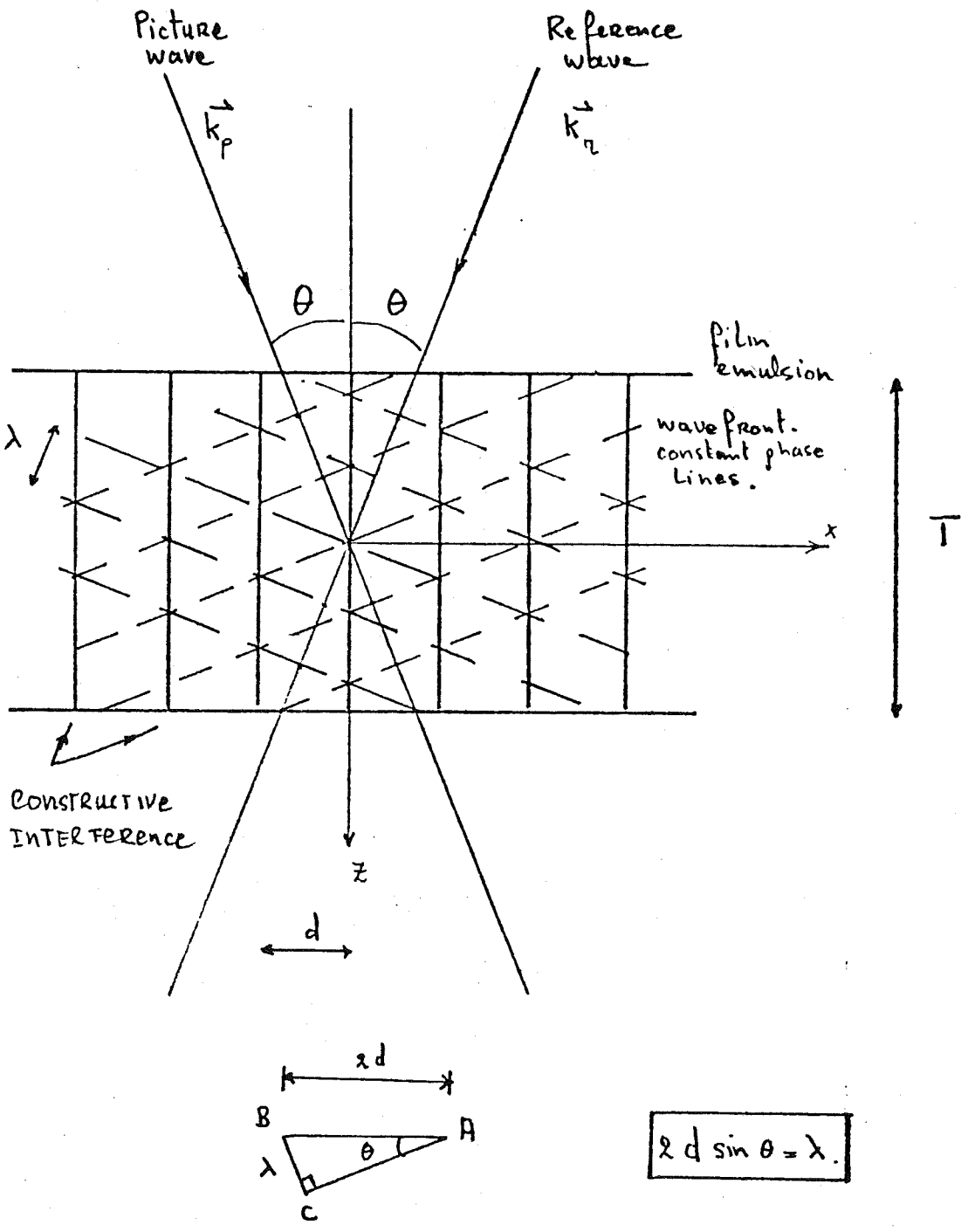


Figure 8.7 Super Position of Two Plane Waves

The fringe spacing is given by $2d \sin \theta = \lambda$. In case the film thickness is thin compared with the fringe spacing the hologram is considered to be plane and if the emulsion thickness T is large compared with d the hologram acts like a volume grating in the reconstruction process. A generally accepted rule is that:

$$T > 1.6 \frac{d^2}{\lambda} \tag{8.9}$$

implies that the hologram acts like a Bragg diffraction element, where T represents the emulsion thickness, d the fringe separation and λ the wavelength during the recording process. The differences in physical properties reveal themselves in the reconstruction process, in particular the diffraction efficiency and orientation sensitivity are widely different for the two holograms. The diffraction efficiency is a measure of the amount of energy that is diffracted into the reconstructed object beam for a given intensity in the reconstruction beam. Plane holograms typically diffract 30% of the incoming energy and volume holograms can diffract 95% or more of the incident energy. The orientation sensitivity is related to the efficiency of the reconstruction process as a function of the orientation of the hologram with respect to the reconstruction beam. Optimum efficiency occurs when the direction of the reconstruction wave is equal to that of the reference wave. Thick holograms are rather sensitive to orientation changes and the efficiency of the reconstruction is strongly influenced by direction of illumination in the reconstruction phase. Plane holograms are not very sensitive to orientation changes and can be illuminated from a large range of angles. Quantitatively, the diffraction process is described by the following laws. Consider again a hologram that is created by the super position of two plane waves. A set of fringes are produced and they are stored in the form of dark and bright bands in the photographic emulsion after development. Upon illumination of this grating or hologram with a reconstruction wave, the object wave is generated if the angle of incidence Ψ, which is measured inside the photographic medium satisfies the Bragg-condition

$$\begin{aligned} 2d \sin \Psi &= \pm \lambda \\ \Psi &= \pm \theta \text{ or } \Psi = \pm (\pi - \theta) \end{aligned} \tag{8.10}$$

where λ is the wavelength of the reconstructed beam measured inside the medium, d is the fringe separation and 2θ is the angle between the plane waves in the construction process.

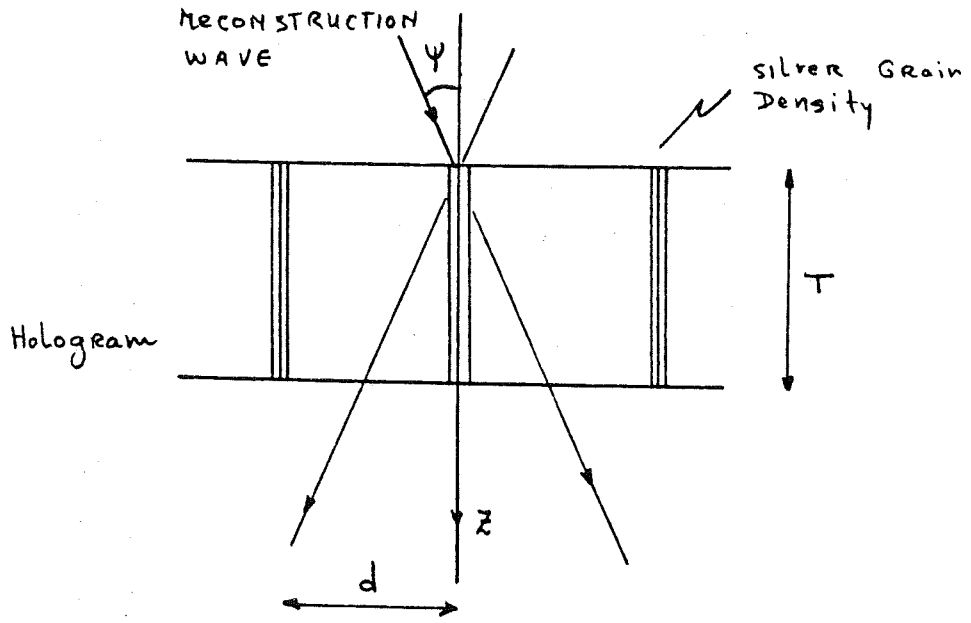


Figure 8.8 Diffraction From A Thick Hologram

The diffraction efficiency depends crucially on Ψ. For a plane hologram the angle Ψ is not very critical and satisfies the relationship:

$$d(\sin \Psi + \sin \phi) = \lambda \qquad (8.11)$$

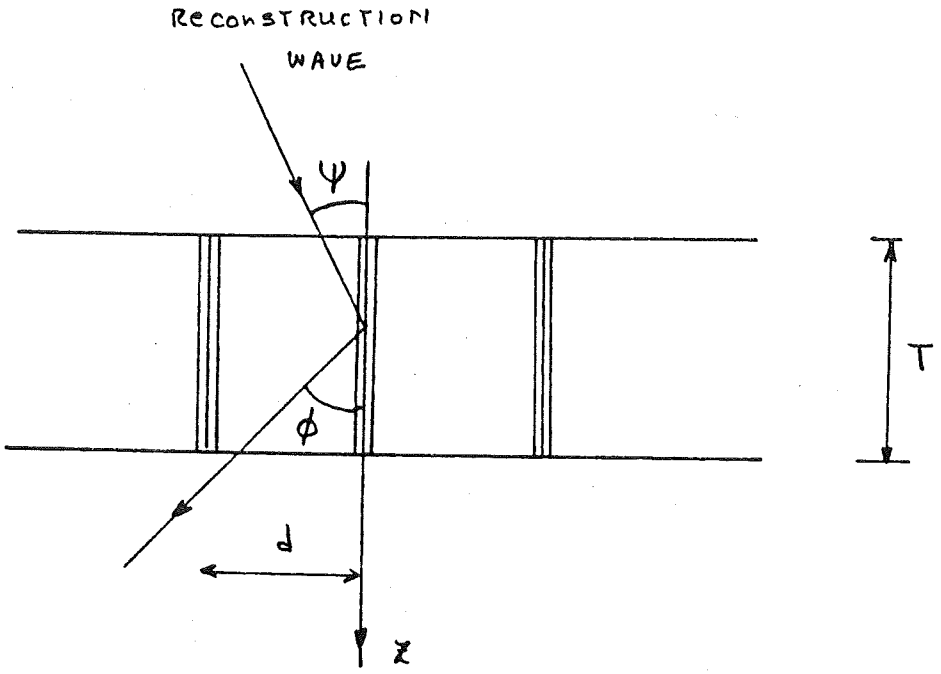


Figure 8.9 Diffraction From A Thin Hologram

The angle ϕ of the diffracted wave is determined by (8.11) given a value of Ψ, d and λ, which again is measured inside the hologram.

In practice the fringe spacing inside the hologram can be controlled by the experimenter by properly choosing the optical arrangement in the recording phase of the experiment. In general the fringe spacing in the hologram is not uniform and certain portions of the hologram act like thin holograms and others like thick holograms. To illustrate this point consider the super position of a point source located at S and a plane wave. The properties of the hologram depend on the location of the film plate and four different positions can be identified.

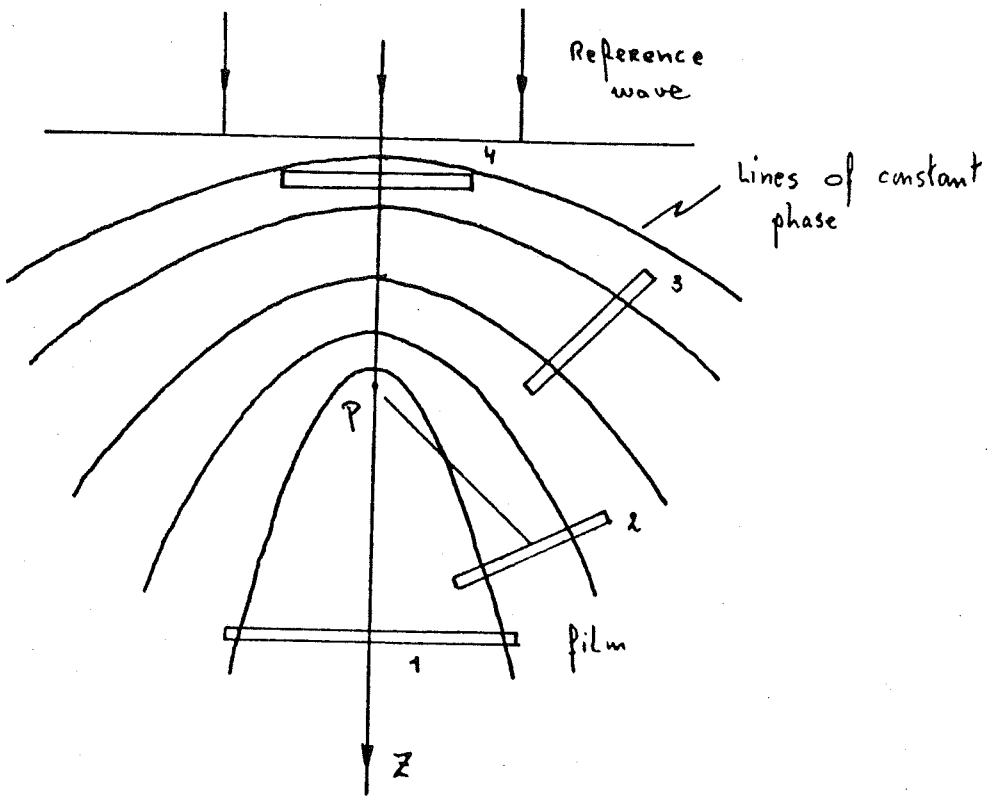


Figure 8.10 Alternative Film Locations
In Reference To The Constant Phase Lines

1. This set up corresponds to Gabor's arrangement in 1948 and is an <u>in-line</u> hologram. The coherence requirements for the light source are low and the relatively large spacing between the fringes implies that the resolution requirements for the film are not severe. This hologram is categorized as a plane hologram.

2. This position corresponds to an <u>off-axis</u> hologram that was first introduced by Leith and Upatnieks in 1962. A laser light source is needed and larger three dimensional objects can be reconstructed. This type hologram is in general considered to be a plane hologram as well.

3. At this location the mean angle between the reference and object waves is in the order of 90° and the hologram acts like a Bragg diffraction grating. This type hologram is often associated with van-Heerden who described it first in 1963.

4. In this configuration the object and reference wave are counter propa-

gating and the separation between fringes is in the order of $\lambda/_2$ and the fringe planes are more or less parallel to the emulsion surface. The emulsion is 12-15 µm thick for a film like Kodak 649F and therefore 50 or more fringes are located within the depth of the sensitive film material. This hologram was first described by Denisyuk in 1962 and is called a reflection hologram. For the reconstruction white light can be used, because the Bragg condition will assume that only that part of the light spectrum that corresponds to the wavelength used during the recording process will be effective in the reconstruction process. The hologram acts like a resonant reflective filter. Lippmann described a similar process around the turn of the century to be used for color photography and this type hologram is therefore often referred to as a Lippmann-Bragg hologram as well.

Finally different recording and reconstruction configurations will be dicussed in class and applications too.

L. Hesselink, Stanford University March 1984

IMAGE RECONSTRUCTION FROM PROJECTIONS

I. STATEMENT OF THE PROBLEM

- Determine the distribution of some physical property, such as density, absorption coefficient, or brightness of an object under investigation.
- Often, a set of line integrals of such distributions can be obtained from appropriate physical measurements. A set corresponding to a particular angular view is called a *projection.*

Example:

Medicine: find the location and shape of a tumor inside a patient's brain. No direct access.

Nondestructive Testing: find flaws, cracks inside a solid material.

Fluid Mechanics: determine the density distribution inside a gaseous jet with combustion.

II. IDEALIZED PROJECTION MEASUREMENT PROCESS.

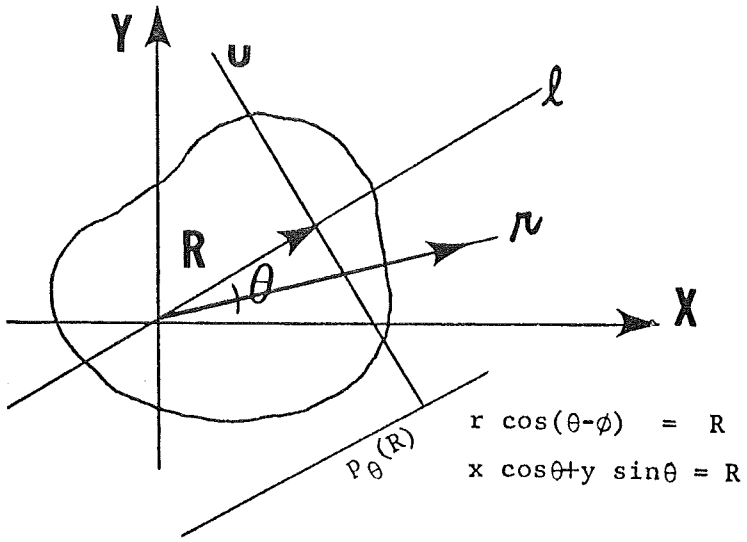


Fig. 1 Recording Geometry

Consider Fig. 1, where:

$g(x,y)$ represents the distribution of the physical property within the object. Assume 2-d.

Projection Data: estimates of line integrals along lines of known location.

u: line along which the line integral of g is taken. u is determined by R, the pathlength and θ.

In terms of R and θ we can compute the path integral along u:

$$p_\theta(R) = p(R,\theta) = \int_{-\infty}^{\infty} g(R\cos\theta - u\sin\theta, R\sin\theta + u\cos\theta)\,du$$

$$= \int_{-\infty}^{\infty} g(x,y)\,\delta(x\cos\theta + y\sin\theta - R)\,dx\,dy \qquad (1)$$

2.1 OBJECTIVE: Determine q from a set of integrals $p(R,\theta)$.

2.1.1 Simplest Case:

Objects with circular symmetry can be reconstructed from projections using an Abel inversion scheme (1826).

2.1.2 General Case:

Radon first solved the problem of reconstructing an object from a series of projections (1917).

2.2 HISTORICAL BACKGROUND:

First reconstructed images were deduced from projection data by astronomers: *R.M. Bracewell, Aust. J. Phys.*, **9**:198, 1956.

Medical Field: Oldendorf, 1961, *IRE Trans.*, **BME-8**:68-72.

Electron Microscopes: delRosier and Klug 120, *Nature*, **217**:130-134, 1968.

Heated Plate Convection Fields: Sweeney and Vest, *Appl. Opt.*, **12**:2649-2664, 1973.

2.3 SEVERAL METHODS:

- Methods that provide wrong results: ART, back-projection.
- Correct Methods: filtered back-projection, convolution back-projection.
- Iterative Approaches

Idea:

Find a two-dimensional distribution which matches all of the projections.

III. The method is called: Algebraic Reconstruction Technique.

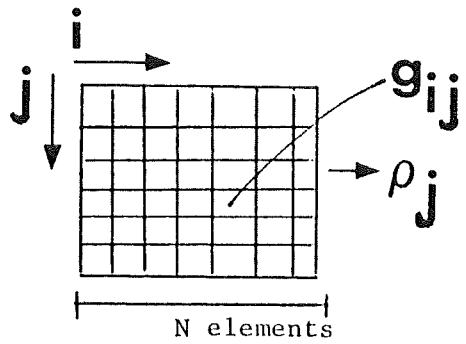


Fig. 2 ART Technique

Consider Fig. 2, where g_{ij} represents elements along the j^{th} line, forming the projection ij, ρ_j. Then the algorithm is:

$$g_{ij}^{q+1} = g_{ij}^{q} + \frac{p_j - \sum_{1}^{N} g_{ij}^{q}}{N}$$

where q = iteration.

Start: Set all values $g_{ij} = 0$; g_{ij} are known.

Example:

12	5	16	9
	$g_1 = 3$	$g_2 = 7$	10
	$g_3 = 2$	$g_4 = 9$	11

All projections are known. Start with all $g_{ij}'s = 0$.

0	0
0	0

vertical rays

$$g_1^1 = g_3^1 = 0 + \frac{5-0}{2} = 25$$

$$g_2^1 = g_4^1 = 0 + \frac{16-0}{2} = 8$$

2.5	8
2.5	8

horizontal rays

$$g_1^2 = 2.5 + \frac{10-10.5}{2} = 2.25 \qquad q_3^2 = 2.5 + \frac{11-10.5}{2} = 2.75$$

$$g_2^2 = 8 + \frac{10^2-10.5}{2} = 7.75 \qquad q_4^2 = 8 + \frac{11-10.5}{2} = 8.25$$

2.25	7.75
2.75	8.25

$$g_3^3 = 2.75 + \frac{9-10.5}{2} = 2 \qquad q_2^3 = 7.75 + \frac{9-10.5}{2} = 7$$

$$g_1^3 = 2.25 + \frac{12-10.5}{3} = 3 \qquad q_4^3 = 8.25 + \frac{12-10.5}{2} = 9$$

QED

For larger formats many iterations may be required. Other variations are possible, including multiplicative ART

$$g_{ij}^{q+1} = \frac{p_j}{\sum_{i=1}^{N} g_{ij}^{q}} g_{ij}^{q}$$

Problems:

- extensive computation time
- convergence accuracy not always good.

Conclusion: Use Direct Methods.

IV. FOURIER TRANSFORM APPROACH

Remember:

$$p_\theta(R) = \int\int g(x,y)\delta(x\cos\theta + y\sin\theta - R)\,dx\,dy$$

$$= \int_0^{2\pi}\int_0^{\infty} g(r,\phi)\delta[r\cos(\theta-\phi)-R]\,r\,dr\,d\phi \qquad (2)$$

where: $p_\theta(r)$ = projection information in the θ-direction. In this calculation we perform integration along $x\cos\theta + y\sin\theta = R$ using polar coordinates r,ϕ and $r\cos(\theta-\phi) = R$. The delta function $\delta(r\cos(\theta-\phi)-R)$ sifts out the desired line to provide a *line* integration.

The following methods are all based on a basic property of **2-D Fourier Transforms:**

Consider $g(x,y)$ and let $G(f_x,f_y) = F\{g(x,y)\}$.

$$G(f_x,f_y) = \int\int g(x,y)e^{-i2\pi[f_x x + f_y y]}\,dx\,dy$$

or in polar coordinates

$$G(f_x,f_y) = G(\rho,\beta) \quad , \quad f_x = \rho\cos\beta \quad , \quad f_y = \rho\sin\beta$$

$$G(\rho,\beta) = \int\int g(x,y)e^{-i2\pi\rho[x\cos\beta + y\sin\beta]}\,dx\,dy$$

$$= \int\int\int g(x,y)\delta(x\cos\beta + y\sin\beta - R)e^{-i2\pi\rho R}\,dx\,dy\,dR \qquad (3)$$

Compare (2) and (3) to get:

$$G(\rho,\beta) = \int p_\beta(R) e^{-i2\pi\rho R}\, dR$$

$$G(\rho,\beta) = F_1\{p_\beta(R)\} \tag{4}$$

Thus the Fourier Transform of a projection at angle β forms a line in the Fourier plane at exactly the same angle β! Thus $\beta \equiv \theta$ as shown in Fig. 3.

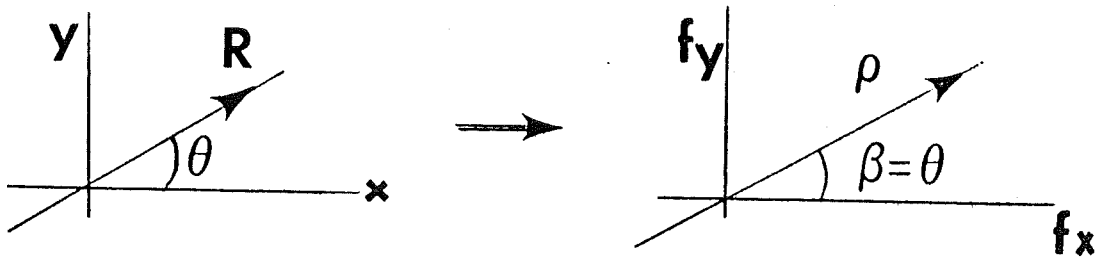


Fig. 3 Coordinate Transformation

Thus the procedure for tomographic reconstruction is:

- Fill the entire plane with projections → the entire Fourier plane is filled.
- Back transform using a 2-D FFT to get $g(x,y)$

$$g(x,y) = \int\int G(fx,fy) e^{i2\pi(f_x x + f_y y)} df_x\, df_y$$

$$= \int_0^{2\pi} d\theta \int_0^{\infty} G(\rho,\theta) e^{i2\pi\rho(x\cos\theta + y\sin\theta)} \rho\, d\rho \tag{5}$$

4.1 EXAMPLE:

$$p_\theta(R) = 2 sinc\, 2R$$

$$P_\theta(R) = F\{p_\theta(R)\} = rect\ \rho/2$$

ρ = one-D variable along line θ = const. Add up all contributions to get

$$F(\rho,\theta) = F(\rho) = circ\,\rho \qquad \text{(pill box)}$$

Then the reconstructed density is represented by:

$$g(x,y) = g(r) = F^{-1}\{cir\rho\} = \frac{J_1(2\pi r)}{r}$$

Problem with Fourier Approach:

- computationally intensive
- need several coordinate transforms.

V. SIMPLE APPROACH: BACK PROJECTION

Idea:

The measured values obtained along each line are projected back along the same line, assigning the measured value at each point in the line.

5.1 EXAMPLE: Consider a δ function at the origin

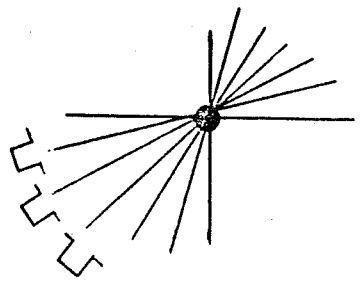


Fig. 4 Delta Function Source at Origin

Algorithm Start: assign measured value along the entire line. We know it is somewhere along the line but we don't know where it is supposed to be located:

$$b_\theta(x,y) = \int_{-\infty}^{\infty} p_\theta(R)\delta(x\cos\theta + y\cos\theta - R)dR$$

where: $b_\theta(x,y)$: back projected density due to projection $p_\theta(R)$ at angle θ. Now, add up the contributions at all angles to get:

$$g_b(x,y) = \int_0^{\pi} b_\theta(x,y)d\theta$$

$$= \int_0^{\pi} d\theta \int_{-\infty}^{\infty} p_\theta(R)\delta(x\cos\theta + y\sin\theta - R)dR \qquad (6)$$

where $g_b(x,y)$: *crude* reconstruction of $g(x,y)$ by pure *back projection.* Such a reconstruction is called a *Laminogram.*

This procedure produces **distortions:** A δ-function $\rightarrow$ $1/r$ spot (impulse response) which we can represent as follows:

$$g_b(x,y) = g(x,y) * \frac{1}{r}$$

Thus high frequency comp are *smeared* out. *Blurring* of the image occurs.

Correction: Take FT and find

$$G_b(\rho,\theta) = \frac{G(\rho,\theta)}{\rho} \rightarrow$$

$$G(\rho,\theta) = \rho G_b(\rho,\theta)$$

Thus: take FT of $G_b(\rho,\theta)$, multiply by ρ and take inverse FT.

Problem: Computationally intensive *2 FFT operations (2-D)* are required.

VI. FILTERED BACK PROJECTION

Objective: Perform back projection and filtering but only 1-D Fourier transforms should be used.

Start with (6)

$$g_b(x,y) = \int_0^{\pi} d\theta \int_{-\infty}^{\infty} p_\theta(r)\delta(x\cos\theta + y\sin\theta - R)\,dR$$

and use (4) $G(\rho,\theta) = F_1\{p_\theta(R)\}$ or

$$p_\theta(R) = F_1^{-1}G(\rho,\theta)$$

$$= \int_{-\infty}^{\infty} G(\rho,\theta)e^{i2\pi\rho R}\,d\rho \qquad (7)$$

Combining (6) and (7) gives

$$g_b(x,y) = \int_0^{\pi} d\theta \int_{-\infty}^{\infty} F_1^{-1}G(\rho,\theta)\delta(x\cos\theta + y\sin\theta - R)\,dR$$

$$= \int_0^{\pi} d\theta \int_{-\infty}^{\infty} \left[\int_{-\infty}^{\infty} G(\rho,\theta)e^{i2\pi\rho R}\,d\rho\right]\delta(x\cos\theta + y\sin\theta - R)\,dR$$

integrate over R

$$= \int_0^{\pi} d\theta \int_{-\infty}^{\infty} G(\rho,\theta)e^{i2\pi\rho[x\cos\theta + y\sin\theta]}\,d\rho$$

Now use (4) to get

$$g_b(x,y) = \int_0^{\pi} d\theta \int_{-\infty}^{\infty} \frac{F_1\{p_\theta(R)\}}{|\rho|} e^{i2\pi\rho[x\cos\theta + y\sin\theta]} |\rho| \, d\rho \tag{8}$$

which produces **distorted** results.

Compare this expression with a 2-D FT technique, which gives good results:

$$g(x,y) = \int_0^{2\pi} d\theta \int_0^{\infty} G(\rho,\theta) e^{i2\pi\rho(x\cos\theta + y\sin\theta)} \rho \, d\rho$$

$$= \int_0^{\pi} d\theta \int_{-\infty}^{\infty} G(\rho,\theta) e^{i2\pi\rho(x\cos\theta + y\sin\theta)} |\rho| \, d\rho \tag{9}$$

Thus to get *good* results we have to multiply the integrand of (8) by $|\rho|$. Equation (8) now implies:

$$g(x,y) = \int_0^{\pi} d\theta \int_{-\infty}^{\infty} \frac{F_1\{p_\theta(R)\} |\rho|}{|\rho|} e^{i2\pi\rho[x\cos\theta + y\sin\theta]} |\rho| \, d\rho \tag{10}$$

Interpretation:

The 1-D FT of the back projection is multiplied by the frequency variable $|\rho|$ to eliminate $\frac{1}{|\rho|}$ blurring!

Thus the 1-D transform of each projection is taken, filtered, inverse transformed and subsequently back projected, because (10) implies

$$g(x,y) = \int_0^{\pi} d\theta \int_{-\infty}^{\infty} \left[F_1\{p_\theta(R)\} |\rho| \, e^{i2\pi\rho R} \right] \delta(x\cos\theta + y\sin\theta - R) \, dR$$

and

$$g(x,y) = \int_0^{\pi} d\theta \int_{-\infty}^{\infty} F_1^{-1}\left[F_1\{p_\theta(R)\,|\rho|\}\right]\delta(x\cos\theta + y\sin\theta - R)\,dR \qquad (11)$$

This procedure implies that we don't have to use Fourier transforms, but can perform convolution operations

$$F_1^{-1}[F_1\{p_\theta(R)\}\,|\rho|] = p_\theta(R) * F_1^{-1}\{|\rho|\} \qquad (12)$$

Thus we convolve with the inverse transform of $|\rho|$.

This process is *computationally very attractive* and the most widely used reconstruction algorithm.

Problem: $C(R) = F_1^{-1}\,|\rho|$ does not exist. Thus we need to use approximations.

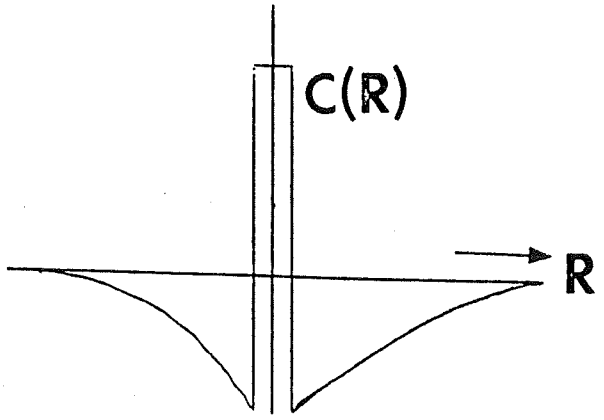


Fig. 5 Convolution Function

In practice systems are bandlimited → the $|\rho|$ filter is of finite extent:

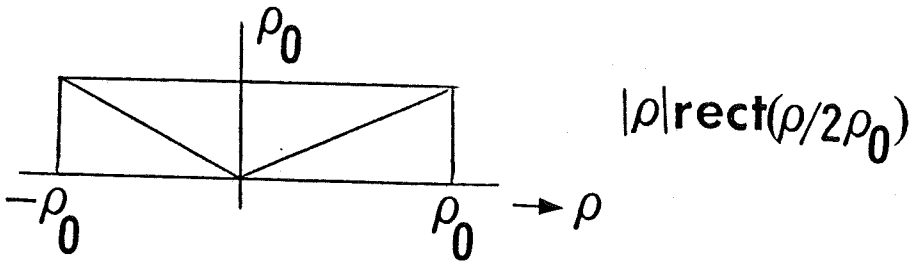


Fig. 6 Convolution Filter

$$|\rho| \, rect \, \frac{\rho}{2\rho_0} = rect \, \frac{\rho}{2\rho_0} - \Lambda\left(\frac{\rho}{\rho_0}\right)$$

and

$$C(R) = F_1^{-1}\{|\rho| \, rect \, \rho/2\rho_0\} = \rho_0[2sinc\,2\rho_0 R - sinc^2\rho_0 R] \qquad (13)$$

Procedure: Take $p_\vartheta(R)$, which is bandlimited, convolve it with (13) and *back project.*

Many filters and convolution fcts have been used. Application dependent.

VII. RECONSTRUCTION OF THE ATTENUATION COEFFICIENT:

In case we make measurements of the attenuation coefficients the formulas have to be modified as follows.

X-ray attenuation: $I = I_0 e^{-\int \mu(z)dz}$

Take log $\frac{I_0}{I} = \int \mu(z)dz$

Then use the formulas presented here.

Ref.: *Image Reconstruction from Projections*, Springer, Berlin 1979. Topics in A. Phys., vol. 32, editor G.T. Hermann.

THREE-DIMENSIONAL TOMOGRAPHIC RECONSTRUCTION OF THE FLOW AROUND A REVOLVING HELICOPTER ROTORBLADE; A NUMERICAL SIMULATION *

ABSTRACT

This paper discusses tomographic data acquisition and reconstruction procedures for determining the flow around a revolving helicopter rotor blade. The data acquisition procedure is simulated using as a testbed a numerical representation of the flow and projections through this known field are computed. We have investigated: a) the effect of the number of projections on the accuracy of the reconstruction, b) the fidelity of the reconstruction when the region of intersection of all projections is smaller than the spatial extent of the flow.

Introduction

The flow around a revolving helicopter rotor blade is three-dimensional in extent and, for the hovering case, stationary in wing fixed coordinates. Knowledge of the density field, including the shock, is of paramount importance for understanding the sound radiated by the helicopter blade. It is difficult to map the density field using point probes and remote (optical) techniques are required. One such method is optical computer assisted tomography (OCAT). The method essentially consists of determining the optical pathlength in several directions. In blade fixed coordinates a parallel beam of laser light is pivoted about a point of rotation in the center of the region of interest.

* Lambertus Hesselink and Ray Snyder, *Proceedings*, Third Int. Symposium on Flow Visualization, Ann Arbor, Michigan, September 1983, pp. 350-357.

Holographic interferograms are recorded in all directions, typically at angular separations of 1 degree and over a total arc of 180 degrees.

The OCAT method is based on inverting a line integral, using many different views of the object, called projections. In general the line integral can be written as

$$Proj(b,\theta) = \frac{2\pi}{\lambda} \int_0^{l(b,\theta)} n(x,z)\, ds \qquad (1)$$

where l denotes the pathlengths through the object, and $n(x,z)$ represents the index of refraction, b and θ denote the radial and angular coordinate respectively, and λ the wavelength of light. Thus each projection represents a line integral, which views the object from a particular direction.

In computerized tomography, using one of the many reconstruction algorithms such as the Fourier transform method[Ref 1], convolution back projection [Ref 2], or ART [Ref 3], a reconstruction is made of the index of refraction $n(x,z)$ in each cross-section. By stacking a series of cross-sections a three-dimensional object can be reconstructed holographically [Ref 4]. A nonlinear filtering operation can then be applied to the reconstructed data in order to emphasize small variations in the index of refraction or equivalently the density.

In this paper we address two aspects of the tomographic method. First, we determine how many projections are needed to reconstruct the object with a prescribed accuracy. The criterion for comparison is the squared difference between the original image and the reconstructed image. Second, we investigate the tomographic reconstruction of only a fraction of the object. In this case the total area of overlap of the projections is smaller than the spatial extent of the object, and it is no longer possible to completely recover the object from the projections and artifacts are introduced.

Simulated recording configuration

Presently facilities are available at the AVRADCOM laboratory at NASA Ames for studying the flow around a revolving helicopter rotor blade. Diagnostic instrumentation includes a pulsed ruby laser holographic interferometer system for measuring optical pathlength. Projections through the flow field around the tip can be obtained by pulsing the light source at various angular positions of the blade and keeping the beam direction fixed in laboratory coordinates (the beam can be moved laterally). It is assumed here that the flow is stationary in wing-fixed coordinates, at least for the hovering case. The beam cross-section and the geometry of the experimental configuration is such that the intersection of all projections is smaller the spatial extent of the tip flow field. Furthermore, only limited-view projections over an arc less than 180 degrees can be measured. We have modeled this configuration numerically on a computer.

As a testbed we used the computed flow field around a revolving helicopter blade. Dr. F. Caradonna has performed these calculations, but several of the simplifying assumptions need to be investigated experimentally. However for the present purpose the results are satisfactory. The flow field is known on a 128x128 mesh grid and we compute projections assuming straight ray propagation as a function of θ as shown in Figure 1. The number of bins or rays per projection is p. The rays propagate in the x-z plane parallel to the plane of rotation at a distance y=0.0593 cordlengths above the wing. By stacking planes a three-dimensional volume can be scanned.

The projections are calculated using a sophisticated program which executes complicated interpolations to compute the actual ray path times the index of refraction (the optical pathlength) through the square mesh grid. We have investigated several reconstruction methods, including the convolution back projection, Fourier transform methods, filtered back projection and iterative procedures. The convolution back projec-

tion method provides the best results, and is computationally efficient. The time required for one reconstruction on a grid of 128x128 elements, using p=200 bins and 90 projections (one every 2 degrees) is 2.16 minutes on our VAX 11/780.

The testbed data field is shown in perspective view in Figure 2. Density is plotted as function of the x-z coordinates in a plane a distance y=0.0593 cordlengths above the rotor blade. The far field density is atmospheric. A perspective 3-D plot of the computed projections is shown in Figure 3. The projection value is plotted vertically as a function of bin position and angle θ. For angles $|\theta| > 40$ degrees the shape of the projection curve can be understood by purely geometric reasoning. The first projection indicates that the optical pathlength, as measured perpendicular to the blade direction at $|\theta| = 90$ degrees is constant at all bins. For decreasing angle $|\theta|$ the rectangular shape of the projection curve transforms into a trapezoid until at $|\theta| = 45$ degrees the projection curve becomes a triangle. This result can be understood by considering the pathlength of rays in a collimated beam propagating through a constant density field of square extent. The projections corresponding to directions between $0 < |\theta| < 45$ degrees cannot be understood on the basis of geometric arguments alone, but depend on the details of the density distribution in the flow field. To emphasize the projections in this range we have plotted in Figure 4 the projections through the *perturbation* field consisting of the difference between the computed local and atmospheric density. These results suggest that not all projections have to be measured in an actual experiment, but only those that cannot be predicted from a-priory information. Of course, this does not imply that the other projections are not important for the reconstruction, on the contrary, but only that those projections can be made zero, thus greatly reducing the data acquisition requirements.

Results

A cross-section through the flow field, taken perpendicular to the span direction at a distance of z=0.95 span is shown in Figure 5. Note that the density increases near the leading edge, than decreases over the blade and subsequently increases again near the trailing edge. The blade extents from -0.5 chord to 0.5 chord. The pressure and density increase occurs across a shock, which propagates approximately radially outward. The curve indicated by original represents a cross-section through the testbed data; the other curves denoted by 40,60,80 and 180 represent cross-sections obtained by limited-view reconstructions over a range of $\theta = \pm$ 20,30,40 and 90 degrees respectively. The projections of the perturbation density are calculated at two degree intervals; the missing projections are presumed to be zero. The results indicate that the reconstruction is very good indeed. Only very small details in the reconstructed field are different from the testbed data using 40 projections over an arc of 80 degrees. Even fewer limited-view reconstructions predict the location of the shock very accurately, but not the amplitude. The root mean squared difference for the reconstructions using 40 views is less than 0.4 % of the atmospheric density and the maximum difference is 5 %. In these calculations the area of intersection of all projections completely covers the flow field of interest, and all density values outside this region correspond to the unperturbed background value.

Figure 5 shows a perspective view of the modified testbed data. Note that the shockwave is extended into the far field and the amplitude of the shock has been kept constant in that region. The area of overlap of the projections is kept the same as used for the reconstruction of the original testbed data (p=200, but much smaller than the total displayed field), and thus the projections in the direction parallel to the extended shock are modified substantially. This can be interpreted as adding, correlated, noise to the projections. The effect of this noise on the limited-view ($|\theta| < 40$ degrees) reconstruction is shown in the perspective plot of Figure 6. The main features are still recog-

nizable but artifacts do appear, in particular the streaks in the far field. A cross-sectional plot of the density field is shown in Figure 7. Note that the shock location is accurately determined, but not the strength and rapidly varying density fluctuations are introduced at the leading and trailing edge of the blade. The range of angles over which the projections are calculated for these reconstructions is again indicated.

Conclusions

In this paper we have discussed a numerical simulation of the tomographic reconstruction of the flow field around a revolving helicopter rotor blade. Calculations provided to us by Dr. Caradonna from NASA Ames are used as a testbed for simulating the data acquisition procedure. The calculations are simplified and based on several assumptions which need to be investigated experimentally. However the data are satisfactory for the present study. We have investigated the number of projections required to reconstruct the flow field with high accuracy and found that only 40 projections spaced at two degree intervals need to be acquired over an arc of 80 degrees symmetrically located around the rotor blade in wing fixed coordinates. The reconstruction is very good indeed and the least squared error is less than 0.4%. Artifacts are introduced if the total area of overlap of the projections is smaller than the spatial extent of the flow field. The reconstruction deteriorates and the location of dominant features such as the shockwave is still accurate but not the strength and artificial, rapidly varying density variations are introduced during the reconstruction procedure.

The present simulation assumes straight line ray propagation, which may not be an accurate assumption in real experiments. In particular projections taken along the shock direction may be different from those calculated. This effect needs to be investigated but perhaps an iterative scheme can be used to reconstruct the flow field. Researchers at NASA Ames are presently engaged in the data reduction of the holographic

interferograms, and the flow field will be reconstructed using these data as soon as they become available.

Acknowledgements

This research is supported by NASA grant NCC 2-188. We are indebted to Dr. F Caradonna from NASA Ames for providing us with the testbed data.

References

1. Bracewell, R.N. Aust. J. Phys. 9: 198, 1956

2. Ramachandran, G.N. and Lakshminarayanan, Proc. Natl. Acad. Sci., USA, 68: 2236, 1971

3. Gordon, R., Bender, R. and Herman, G.T., J. Theor. Biol., 29: 471, 1970

4. Hesselink, L, Johnson, K.M., and Perlmutter, R Holographic display devices, Invited lecture, Proc SPIE, 403, Geneva 1983 (to be published)

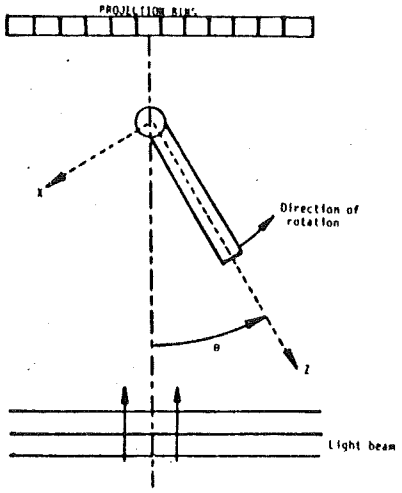


Figure 1. Data acquisition configuration.

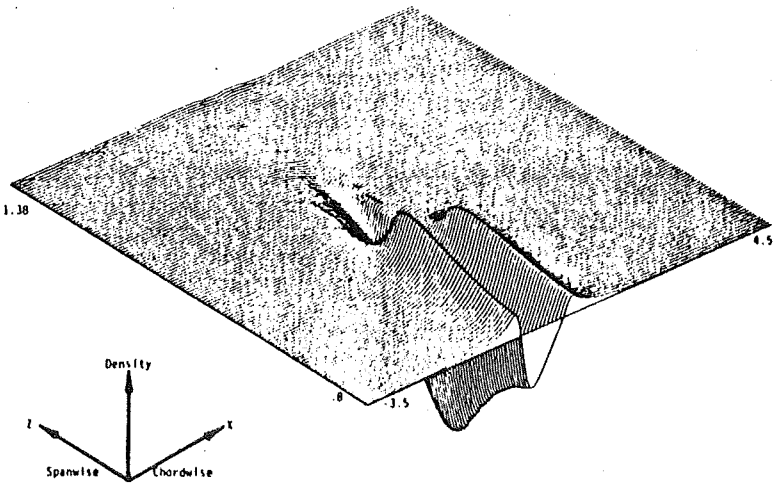


Figure 2. Test bed flow field.

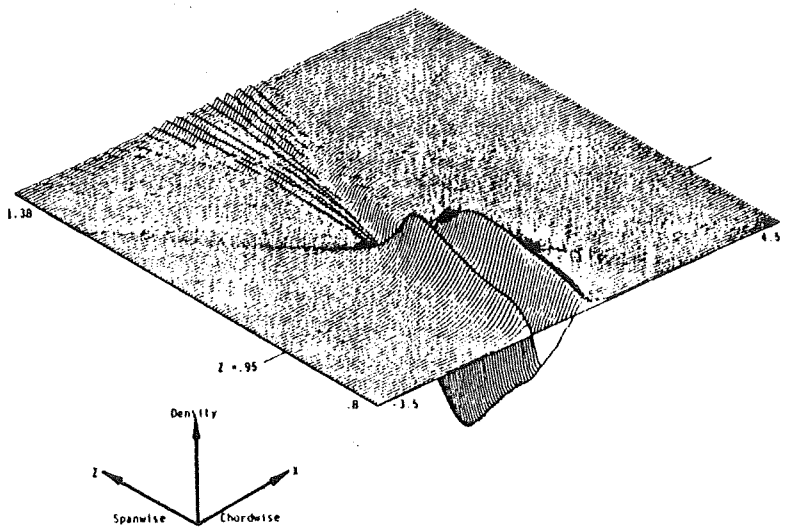


Figure 3. Limited view reconstruction of the test bed flow field using 40 projections at 2 degree intervals ($-40 \leq \theta \leq 38$).

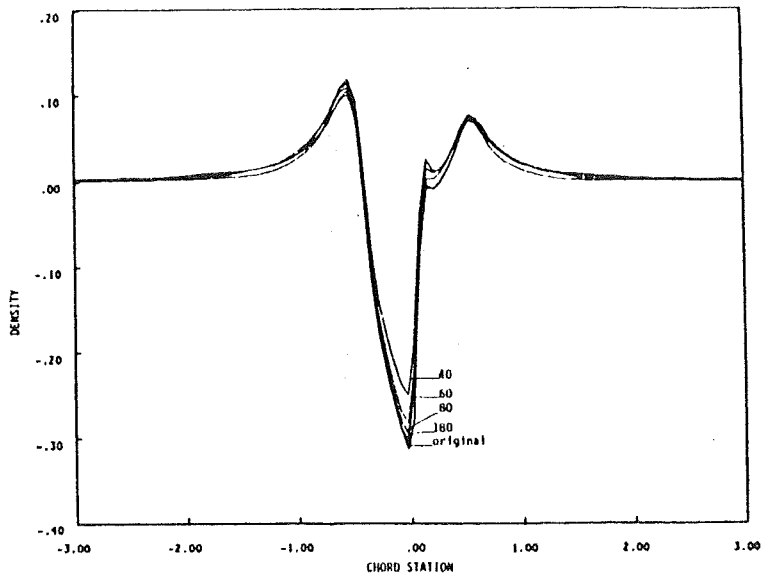


Figure 4. Cross-sections through the (limited-view reconstruction) flow field at a distance of Z = 0.95 span.

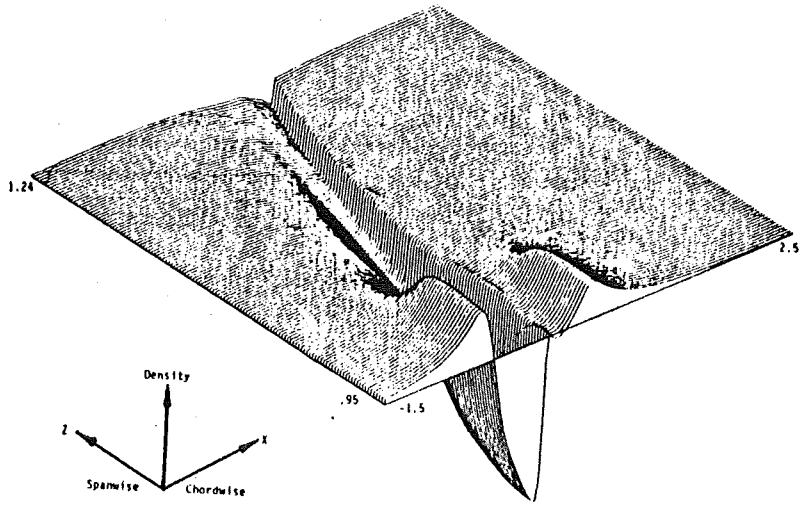


Figure 5. Extended test bed flow field.

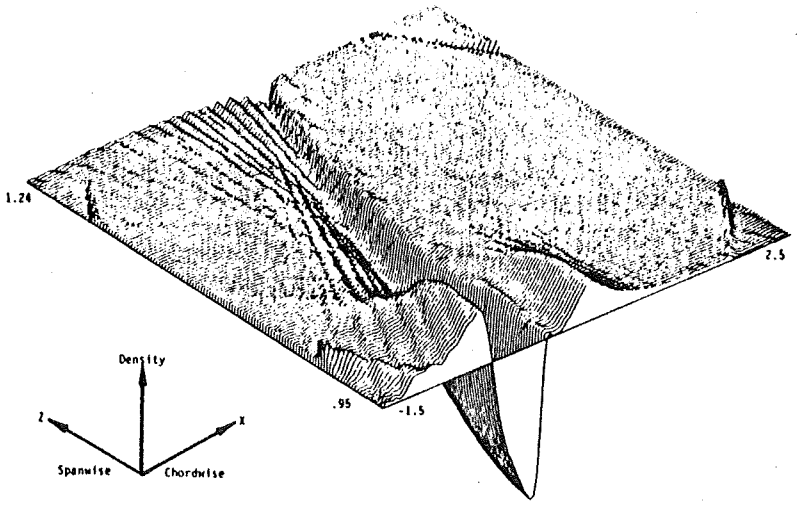


Figure 6. Limited-view reconstruction of the extended test bed flow field using 40 projections at 2 degree intervals ($-40 \leq \theta \leq 38$).

L. Hesselink, Stanford University March 1984

FLUID DYNAMICS APPLICATIONS

In this section we discuss several applications of optical and digital image processing techniques in fluid mechanics research. First, a recent development in real-time holography is discussed. Holography in the classical sense as described in a previous section involves the use of photographic film, which can only be used once. Therefore, real-time recording and reconstruction systems cannot be made using film. Yet there are many applications for which we would like to have a dynamic recoring medium so that results of holographic measurements can be obtained in real-time and continuously. Such applications include deformation studies of solid objects, two-phase fluid flows seeded with bubbles, to mention just a few examples. Recently (Ref. 1), photorefractive recording materials such as $Bi_{12}SiO_{20}$ (BSO), $BaTiO_3$ and $Ba_xSr_{1-x}Nb_2O_6$ (SBN) have been used to dynamically record holograms, and read them out simultaneously by a three-wave interaction process which produces a fourth or phase-conjugate output beam. Such a system has proven to be very useful for holographic interferometry studies and for correction of wavefront aberrations associated with laser propagation through the turbulent earth's atmosphere.

Second, we discuss the use of digital and optical image processing techniques to obtain quantitative information about statistical quantities such as the correlation function or spectrum of a turbulent density field. The method involves obtaining a shadowgraph photograph of a turbulent density field, then digitizing the photograph and subsequently processing the data in a digital computer. The 2-D spectrum of the light intensity fluctuation on the photograph is computed and using an analytical inversion scheme the 3-D spectrum of the index-of-refraction or density fluctuation in the medium can be obtained, assuming that the fluid fluctuations are statistically homogeneous and isotropic.

Third, we discuss a method by which the 3-D topology of a fluid interface, say between two reacting species in a combusting flow may be obtained from a stack of 2-D cross sections. The method comprises of illuminating a flow seeded with scattering particles with a sheet of laser light and recording the scattered radiation on movie film. Either the sheet is translated throughout the volume of the flow in a time so short that no changes take place in the fluid during the recording time, or the fluid convects through the sheet and a Galilean transformation is needed to transform time into space. Subsequently the images are digitized and processed in a digital computer. Projections through the data field are computed and video stereo pairs are used to obtain 3-D topology information. This method provides for interactive data analysis and, using the same algorithms, archival storage can be achieved by generating a multiplex hologram from the digital data.

REAL-TIME HOLOGRAPHY

Several nonlinear optical materials exhibit photorefractive behavior. Upon illumination by a spatially varying intensity field an internal space-charge field is generated, which in turn modifies the index of refraction through the (linear) electro-optic effect. The internal field can be quite large, on the order of 10^5 v/m and index variations of 10^{-3} may be achieved. Photorefractive materials can thus be used for recording holograms. A typical experimental configuration is shown in Figure 1.

Two recording beams, a reference and object wave, are incident on BSO and form an interference pattern throughout the volume of the material. Through the photorefractive effect a hologram is recorded which is read-out by a counterpropagating pump beam and antiparallel to the reference wave. Consequently a fourth counterpropagating or phase conjugate object beam is generated.

Phase conjugation or real-time holography has been used in a diverse field of applications. Examples include: real-time holographic interferometry, wavefront aberration correction, wavefront amplification, logic operations, edge detection, correlation and convolution operations, and pattern recognition. During the workshop several of these examples will be discussed in detail.

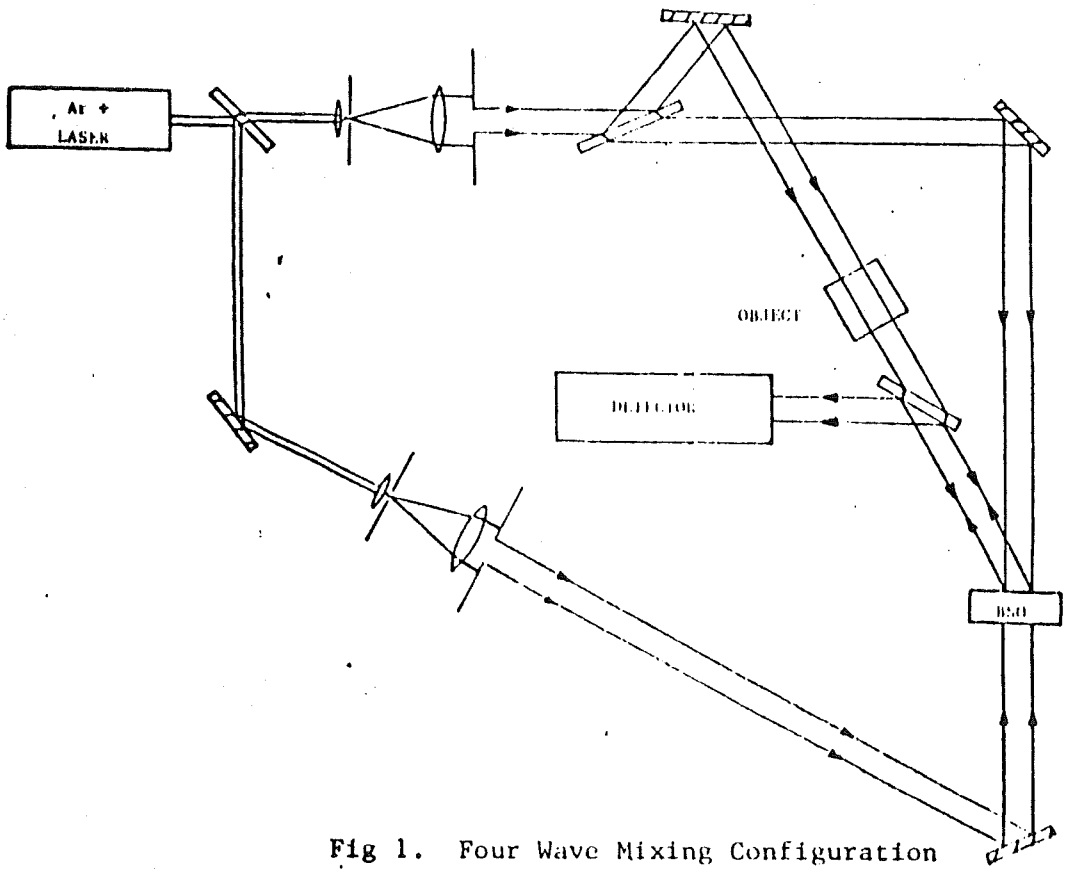


Fig 1. Four Wave Mixing Configuration

Reference

1. Fischer, R. A., Optical Phase Conjugation, Academic Press, 1983.

QUANTITATIVE THREE-DIMENSIONAL FLOW VISUALIZATION *

ABSTRACT

This paper discusses a novel technique for obtaining quantitative three-dimensional flow measurements. The method is applied to a particle laden wake flow behind a circular cylinder. A sheet of laser light illuminates a cross-section of the wake perpendicular to the mean flow direction. Scattered radiation is recorded on high speed film and a time sequence comprising 23 frames is digitized using a scanning microdensitometer. Projections through the data are computed digitally and video stereo pairs as well as a multiplex hologram are synthesized from the projections. Image processing techniques are used to emphasize structures of interest and to address the cloud-within-a-cloud problem. The multiplex hologram is corrected for time-smear effects.

Introduction

Most problems of interest in fluid mechanics research are characterized by three space coordinates and often time. Thus diagnostic techniques for making four-dimensional measurements are highly desirable. Very few such techniques exist at present. Holography provides three-dimensional information, but time dependent information is hard to obtain. The method requires coherent radiation (at least at present), which restricts applicability to diffusively scattering objects.

We have investigated a technique that can provide four-dimensional data and is generally applicable. The method consists of four steps: First, cross-sectional data are

* Lambertus Hesselink, John Pender, Stephen M. Jaffey and Kalyan Dutta,
Proceedings, Third Int. Symposium on Flow Visualization, Ann Arbor, Michigan, September 1983, pp. 375-380.

obtained by sampling and quantizing the flow field in equally spaced parallel planes as a function of time. Second, the data are processed in a digital computer. Image processing techniques are invoked to emphasize details of interest or remove unwanted information. Third, projections through the three-dimensional data base are computed and recorded as gray scale images onto film. Fourth, the projection data are used as input to a hologram recording device to generate a multiplex hologram. The hologram has a 120 degree viewing angle which allows four-dimensional or time-varying data to be presented.

Experimental configuration

The experimental configuration is shown in Figure 1. A circular cylinder is placed perpendicular to a uniform flow field and smoke particles are introduced through slots at plus and minus 30 degrees from the stagnation line. The wake of the cylinder is illuminated by a sheet of laser light oriented perpendicular to the mean flow direction. Radiation scattered from the smoke laden air flow is recorded on high speed motion film. The recorded images represent cross-sections of the flow field convected through the stationary sheet.

Twenty three images are selected from the movie, representing one cycle in the shedding sequence. The images are digitized on a 512x512 grid using a Perkin Elmer model 1010A scanning microdensitometer and the data are stored on tape for further processing. The digital numbers thus represent particle concentrations assuming isotropic scattering. In this experiment the particle size is kept small enough to insure negligent discrepancy between particle and fluid motion.

The individual cross-sections represent slices through the flow field convected past the laser sheet. Invoking a Galilean transformation time is converted into space. This transformation assumes that the flow structure remains unchanged during the time span

considered. This assumption is not necessarily true and the laser sheet should be scanned through the fluid in a time short compared with the time over which the fluid topology changes substantially. This can be done rather straightforwardly using commercially available optical and electronic components, but the added complexity was avoided during these first experiments.

The digital data are computer processed to reveal important information. A sobel operator is applied to the data to extract edges. Often opaque data at the surface of the object can obscure information at the interior. We refer to this problem as the cloud-within-a-cloud problem. The edge enhanced images allow transparency and objects in the interior can be visualized more easily. Other processing such as filtering and pattern recognition can be applied as well during this step in the procedure. Subsequently the data are processed for display using a multiplex hologram.

Three-dimensional data are only useful to a human observer if they can be displayed with true depth perception. Stereo pairs provide three-dimensional depth cues, but only from one perspective. Several other techniques, including those based on the vibrating mirror concept and motion parallax can be used, but do not provide the large viewing angle afforded by multiplex holography (Ref 1). The data reduction procedure required for generating multiplex holograms has been reported previously (Ref 2), but will be repeated here briefly.

Projections through the data are computed by calculating a path integral along straight lines as indicated in Figure 2. Each point along the line is considered to be a source proportional to the value of the intensity at that point (or obtained by interpolation from adjacent pixels) The radiation coming from each source point is then attenuated along the path between the source and the observer. The attenuation coefficient can be adjusted to suit the display. Strong absorption implies that only

features on the surface can be seen. This source-attenuation model is used to construct 360 views, separated by 1/3 degree angularly. Each 2-D projection of the 3-D data are displayed on a flat CRT screen and recorded on 35 millimeter film. These images form the input to a holographic recording device for generating a multiplex hologram. Alternatively, stereo pairs can be computed from the 3-D data and displayed on a CRT screen. By rotating the object and viewing stereo pairs motion parallax provides powerful depth cues. An example of this technique will be demonstrated during the conference.

A multiplex hologram is synthesized by imaging each projection, using anamorphic optics, onto a narrow slit in front of holographic film as shown in Figure 3. The imaging optics consists of a spherical and cylindrical lens combination. The slit is a few millimeters wide and approximately 12 inches long. The cylindrical lens focuses the image onto the slit and the spherical lens focuses a distance of a few feet behind the film. Simultaneously a reference wave is superimposed to create a hologram. After exposure the slit is translated one slit width and the next projection is recorded. In this fashion 360 holograms are recorded on film, each representing one projection. Upon illumination of the cylindrical hologram with white light as shown in Figure 4, an observer can view the object with horizontal depth parallax. By moving about the hologram the object can be viewed as a function of time, thus providing four-dimensional information. Four dimensional information can only be included properly by applying time-smear correction, a technique described in Reference 3.

Conclusions

In this paper we have presented a method for analyzing and displaying a three-dimensional flow field at several instances in time. The method provides three-dimensional depth cues to a human observer and a means to compare several data bases

simultaneously. Thus experimental and computational data could be compared with this technique. The advantages are:

- Any input data can be used, including fluorescent data, scattering data and numerically generated data.
- Image processing techniques can be used to alleviate the cloud-within-a-cloud problem.
- Four-dimensional data can be presented.
- Data acquisition can be made very fast, allowing turbulent flow fields to be measured.

At present the method is not interactive, since the hologram is recorded on photographic film, however we are presently working in our laboratory to develop real time capabilities. Of course, the stereo video display is interactive, but with a long time constant.

Acknowledgement

This work was supported under AFOSR grant F49620-83-K-0004. The use of Professor B.J. Cantwell's flow facility is gratefully acknowledged.

References

1. Hesselink, L, Johnson, K.M., and Perlmutter, R Holographic display devices, Invited lecture, Proc SPIE, 403, Geneva 1983 (to be published)
2. Stover, H, True three-dimensional display of computer data, Proc SPIE 367, p 141, 1982
3. Dutta, K and Jaffey, S.M. Time smear corrected multiplex holographic display of computorized tomography data, Proc SPIE, 402, 1983 (to be published)

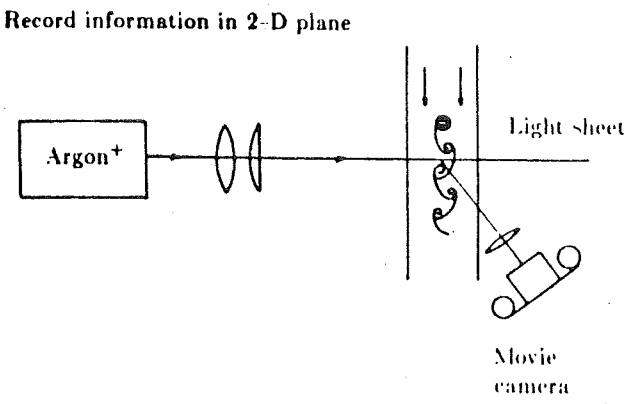


Figure 1. Data acquisition configuration.

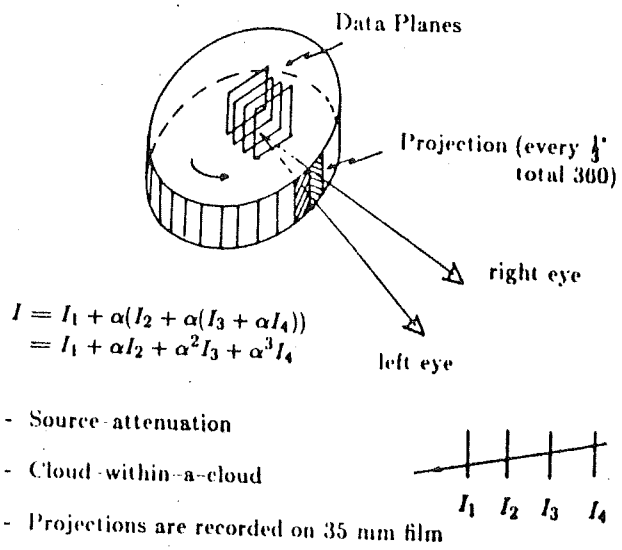


Figure 2. Computer calculation of projections.

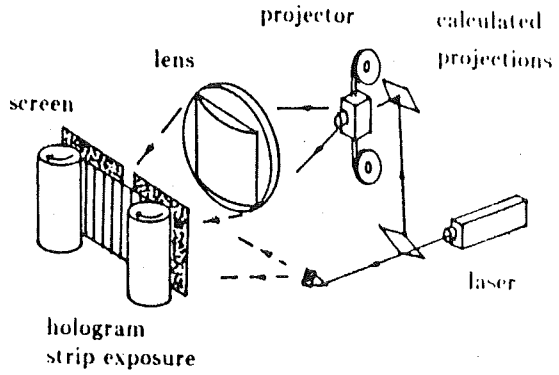


Figure 3. Synthesis of multiple hologram.

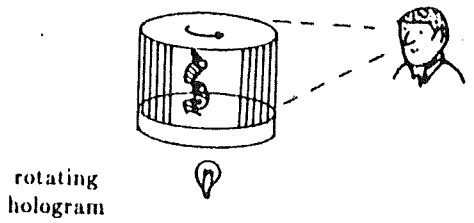


Figure 4. Viewing configuration.

DIGITAL IMAGE PROCESSING OF FLOW VISUALIZATION PHOTOGRAPHS *

ABSTRACT

This paper is concerned with the propagation of laser light through a slab of a randomly varying medium. A theoretical analysis is presented, which relates the spectrum of the recorded intensity field some distance downstream of the medium to the spectrum of the index of refraction field. For a homogeneous and isotropic random field the three-dimensional spectrum of the medium is obtained from the two-dimensional spectrum of the photograph by dividing each component of the spectrum by the frequency raised to the fourth power. Free space propagation outside the random medium is accounted for by a scaling factor. Experimental results are presented which support the theoretical analysis. The non intrusive diagnostic technique presented here is applicable to photographs which contain caustics.

I. INTRODUCTION

Flow visualization studies have played and continue to play an important role in fluid mechanics research. As a prominent case in point the shadowgraph photographs of large scale structures in turbulent shear flows, obtained by Brown and Roshko [Ref 1], have stimulated many workers in the field. The problem of turbulence has received renewed attention and coherent structures in shear flows are intensively studied. Yet, despite the almost universal acceptance of flow visualization studies, only a few attempts

---

* Lambertus Hesselink and Benjamin White,
Applied Optics, Vol. 22, No. 10, May 15, 1983, pp. 1454-1461.

have been made to obtain quantitative information from photographs. The problem that one has to solve belongs to a general class of problems, called *inverse problems*, in which properties of the scattering or refracting medium are determined from properties of the radiation that has been scattered or diffracted by that medium. The main difficulty arises from the fact that at any observation point the scattered radiation depends on the optical properties of the medium everywhere along the raypaths that propagate through that point. Therefore, in order to obtain point resolved information about the object, one has to invert a line integral, which in general can only be carried out for a very restricted class of problems, which exhibit sufficient symmetry. In some cases it is possible, however, to obtain statistical information from the scattered radiation field. Uberoi and Kovasznay [Ref 2] were one of the first investigators to report a data reduction scheme relevant to fluid mechanics research. They took shadowgraph photographs of a homogeneous and isotropic turbulent density field and by using an optical processor they determined the correlation function of the intensity field of the scattered radiation , which was recorded on photographic film. The method essentially consists of preparing two transparent copies of the shadowgraph photograph and positioning them back-to-front in a parallel beam of light. The transmitted field is incident upon a converging lens and the intensity of the light is measured in the back focal plane of the lens as a function of the displacement of one of the transparencies with respect to the other. Invoking the premises of statistical homogeneity and isotropy, they showed that length scales related to the the correlation function of the medium can be obtained from the correlation function of the light intensity fluctuations on the photograph. They found that results obtained for the microscale of the turbulence were in fair agreement with results obtained using hot wires, but that the integral scale could not be computed accurately using this technique. Taylor [Ref 3] extended the Uberoi and Kovasznay

method to include more general recording configurations, but no essentially new results where obtained. Tatarski [Ref 4], in his treatise on wave propagation through turbulence, has studied the propagation of light through such a medium; while he has not directly treated the inverse source problem, our results are basically an extension of his.

In this paper we report on a method for obtaining statistical information regarding a spatially confined random index-of-refraction field from shadowgraph data. A laser is used as a light source and digital image processing techniques are implemented to reduce the data that have been obtained by scanning the photograph with a microdensitometer. In particular we have computed the three-dimensional power spectrum of the medium from the two-dimensional spectrum of the intensity fluctuations on the film.

II. THEORETICAL BACKGROUND OF THE METHOD

A perturbation analysis is applied to the wave equation to yield a solution for the scalar component of the field in terms of the initial conditions,the statistical description of the medium and the propagation distance. The relevant equation is represented by

$$\Delta \hat{u} + k^2 (1 + \epsilon\mu)^2 \hat{u} = 0 \tag{1}$$

where $k = \omega/c$ is the wavenumber,$\hat{u} = \frac{u}{A}$ is a normalized scalar component of the electromagnetic field u with amplitude A, ω is the angular frequency of the wave, and $n = n(x,y,z) = 1 + \epsilon\mu(x,y,z)$ represents the index of refraction, ϵ is a small nondimensional parameter, and μ represents a homogeneous and isotropic random field with zero mean value. The field has a harmonic time dependence that is given by the term $\exp(-i\omega t)$. The propagation direction is along the z-axis of a cartesian coordinate system located at the entrance plane of the random medium.

The problem under consideration is schematically indicated in Figure 1. A plane wave is incident upon a region with a random index of refraction distribution of thickness D. A photographic plate is located a distance $z = \hat{D}$ from the entrance plane. After propagation through the random medium the wave propagates over a distance of $d = \hat{D}\text{-}D$ through free space.

First we set out to compute the wavefield at the plane $z = \hat{D}$. The wave equation is given by (1) and the boundary condition for a plane wave of unit amplitude is

$$\hat{u}(x,y,0) = 1 \tag{2}$$

The image on the film is modelled by the following process:

$$\begin{aligned} I(x,y,z) &= B \int_0^T |\hat{u}(t,x,y,z)|^2 \, dt \\ &= B\,T\,|\hat{u}|^2 \end{aligned} \tag{3}$$

where T represents the exposure time and B is a constant that depends on the film and the development process. Other models for the recording process are possible, in particular for a first order system we may write

$$\begin{aligned} I(x,y,z) &= B \int_{t-T}^{t} U(t - t') \, e^{-\beta(t - t')} \, |\hat{u}(t,x,y,z)|^2 \, dt' \\ &= \frac{B}{\beta}\left[1 - e^{-\beta T}\right] |\hat{u}|^2 \\ &= B\,T'\,|\hat{u}|^2 \end{aligned} \tag{4}$$

where β is a constant and U represents the Heaviside function. Thus equation (4) is not essentially different from (3) in the sense that in both representations the intensity on the film is proportional to the square modulus of the field;therefore ,in this paper we restrict ourselves to the model expressed by equation (3).

The relevant parameters in the analysis need to be examined in order to determine the relative magnitude of each one.The numerical values are given by:

$$\begin{aligned} \epsilon &= 3\ 10^{-5} \\ \omega &= 3\ 10^{15} \\ k &= 10^{5}\ \ cm^{-1} \\ c &= 3\ 10^{10}\ \ cm/\mathrm{sec} \\ D &= 26\ \ cm \end{aligned} \tag{5}$$

For the perturbation analysis let $\epsilon \rightarrow 0$ and let $k \rightarrow \infty$ in the wave equation (1). Furthermore, we introduce the geometrical optics ansatz [Ref 5]:

$$\hat{u} \sim e^{ik\phi(x,y,z)} \sum_{n=0}^{\infty} k^{-n}\ V^{(n)}(x,y,z) \tag{6}$$

and let $\epsilon = \alpha/k$, where α is a proportionality constant of order one. Substitute the expressions for ϵ and $\hat{u}$ into the wave equation and equate the coefficients of k^2, k^1 and k^0 to zero to obtain three equations for ϕ, $V^{(0)}$ and $V^{(1)}$. The result becomes, neglecting reflections at the interface

$$I(x,y,\hat{D}) = A^2BT\{1 - \alpha \int_0^{\hat{D}} dz \left\{(\hat{D} - z)\left(\frac{\partial^2}{\partial x^2} + \frac{\partial^2}{\partial y^2}\right) + \frac{\partial}{\partial z}\right\}\mu(x,y,z))$$
$$+ O(\frac{1}{k^2}) \tag{7}$$

where $I(x,y,\hat{D})$ represents the recorded intensity pattern at plane $z = \hat{D}$.

The statistical properties of the intensity pattern on the photograph can now be related to the statistical properties of the medium as follows. Let the expected value of I be given by

$$E\{I(x,y)\} = A^2BT \tag{8}$$

and let

$$\rho = \sqrt{(x_1 - x_2)^2 + (y_1 - y_2)^2}$$

be the distance between two points $P(x_1,y_1)$ and $Q(x_2,y_2)$. The correlation function of the intensity pattern is then given by

$$\begin{aligned} R_I(\rho) &= E[(I(x_1,y_1) - A^2BT)(I(x_2,y_2) - A^2BT)] \\ &= \left(\frac{\alpha A^2 BT}{k}\right)^2 \int_0^D dz_1 \int_0^D dz_2 \left\{(\hat{D}-z_1)\left(\frac{\partial^2}{\partial x_1^2}+\frac{\partial^2}{\partial y_1^2}\right)+\frac{\partial}{\partial z_1}\right\} \cdot \\ &\qquad \left\{(\hat{D}-z_2)\left(\frac{\partial^2}{\partial x_2^2}+\frac{\partial^2}{\partial y_2^2}\right)+\frac{\partial}{\partial z_2}\right\} \cdot \\ &\qquad \left\{E[\mu(x_1,y_1,z_1)\mu(x_2,y_2,z_2)]\right\} \end{aligned} \tag{9}$$

Again, we set $\Delta_\rho = \frac{1}{\rho}\frac{\partial}{\partial \rho}\rho\frac{\partial}{\partial \rho}$. Then using $\beta = \left(\frac{\alpha A^2 BT}{k}\right)^2$ equation (9) becomes

$$R_I(\rho) = \beta \int_0^D dz_1 \int_0^D dz_2 \left\{(\hat{D}-z_1)\Delta_\rho + \frac{\partial}{\partial z_1}\right\}\left\{(\hat{D}-z_2)\Delta_\rho + \frac{\partial}{\partial z_2}\right\} R\left(\sqrt{\rho^2+(z_1-z_2)^2}\right) \tag{10}$$

We set $z_i' = \hat{D} - z_i$ in (11) and drop primes to get

$$R_I(\rho) = \beta \int_{\hat{D}-D}^{\hat{D}} dz_1 \int_{\hat{D}-D}^{\hat{D}} dz_2 \left\{z_1\Delta_\rho - \frac{\partial}{\partial z_1}\right\}\left\{z_2\Delta_\rho - \frac{\partial}{\partial z_2}\right\} R\left(\sqrt{\rho^2+(z_1-z_2)^2}\right) \tag{11}$$

Therefore (using symmetry)

$$\begin{aligned} R_I(\rho) &= 2\beta\Delta_\rho^2 \int_{\hat{D}-D}^{\hat{D}} dz_1 \int_{\hat{D}-D}^{z_1} dz_2 \; z_1 \; z_2 \; R\left(\sqrt{\rho^2+(z_1-z_2)^2}\right) \\ &-2\beta\Delta_\rho \int_{\hat{D}-D}^{\hat{D}} dz_1 \int_{\hat{D}-D}^{\hat{D}} dz_2 \; z_1 \frac{\partial}{\partial z_2} R\left(\sqrt{\rho^2+(z_1-z_2)^2}\right) \\ &+\beta \int_{\hat{D}-D}^{\hat{D}} dz_1 \int_{\hat{D}-D}^{\hat{D}} dz_2 \frac{\partial^2}{\partial z_1 \partial z_2} R\left(\sqrt{\rho^2+(z_1-z_2)^2}\right) \end{aligned} \tag{12}$$

In the second and third terms of (13) we integrate out over z_2. In the first term, we make the change of variables after which we can integrate out over ξ

$$\left\{\begin{array}{l} \xi = z_1 + z_2 \\ z = z_1 - z_2 \end{array}\right\} \quad \text{and} \quad \left\{\begin{array}{l} z_1 = \frac{1}{2}(\xi + z) \\ z_2 = \frac{1}{2}(\xi - z) \end{array}\right\}$$

The Jacobian is

$$J = \frac{\partial(\xi, z)}{\partial(z_1, z_2)} = \begin{vmatrix} 1 & 1 \\ 1 & -1 \end{vmatrix} = -2.$$

Then

$$\begin{aligned} R_I(\rho) = {} & 2\beta\Delta_\rho{}^2 \int_0^D dz \int_{2\hat{D}-2D+z}^{2\hat{D}-z} d\xi \ \frac{1}{4}\left(\xi^2 - z^2\right) \cdot \frac{1}{2} R\left(\sqrt{\rho^2+z^2}\right) \\ & -2\beta\Delta_\rho \int_{\hat{D}-D}^{\hat{D}} dz_1 z_1 \left[R\left(\sqrt{\rho^2+(\hat{D}-z_1^2)}\right) - R\left(\sqrt{\rho^2+(\hat{D}-D-z_1^2)}\right)\right] \\ & +\beta \int_{\hat{D}-D}^{\hat{D}} dz_1 \frac{\partial}{\partial z_1}\left[R\left(\sqrt{\rho^2+(\hat{D}-z_1^2)}\right) - R\left(\sqrt{\rho^2+(\hat{D}-D-z_1^2)}\right)\right] \end{aligned}$$

The result is

$$\begin{aligned} R_I(\rho) = {} & \frac{1}{4}\beta\Delta_\rho{}^2 \int_0^D dz \left[\frac{\xi^3}{3} - z^2\xi \right]_{\xi=2\hat{D}-2D+z}^{2\hat{D}-z} R\left(\sqrt{\rho^2+z^2}\right) \\ & -2\beta\Delta_\rho \left\{ \int_0^D dz(\hat{D}-z) R(\sqrt{\rho^2+z^2}) - \int_0^D dz(z+\hat{D}-D) R\left(\sqrt{\rho^2+z^2}\right)\right\} \qquad (13) \\ & +\beta\left\{ R(\rho) - R(\sqrt{\rho^2+D^2}) - R(\sqrt{\rho^2+D^2}) + R(\rho)\right\} \end{aligned}$$

Upon evaluation of the first term in square brackets in equation (13), the final result becomes

$$\begin{aligned} R_I(\rho) = {} & \beta\Delta_\rho{}^2 \int_0^D dz \left\{ \frac{(\hat{D}-z)^2(2D+z)}{3} + 2\hat{D}(\hat{D}-D)(D-z)\right\} R\left(\sqrt{\rho^2+z^2}\right) \\ & -2\beta\Delta_\rho \int_0^D dz\,(\hat{D}-2z)\, R\left(\sqrt{\rho^2+z^2}\right) \qquad (14) \\ & +2\beta\left(R(\rho) - R(\sqrt{\rho^2+\hat{D}^2})\right) \end{aligned}$$

where

$$\beta = \left\{ \frac{\alpha A^2 BT}{k} \right\}^2;$$

$$R(|\underline{r}|) = E\{\mu(\underline{x})\,\mu(\underline{x}+\underline{r})\} \qquad (15)$$

$$\Delta_\rho = \frac{1}{\rho}\frac{\partial}{\partial\rho}\rho\frac{\partial}{\partial\rho}$$

The power spectrum of the image, $S(q)$, is the (order zero) Hankel transform of $R(\rho)$. The power spectrum of a two-dimensional planar slice of the medium is now easily computed to be

$$S(q) = \gamma\frac{S(q)}{q^4} + \int_q^\infty K(q,\xi)\, S(\xi)\, d\xi \tag{16}$$

where S is the Hankel transform of $\beta R(\rho)$,q is the frequency and

$$K(q,\xi) = \xi[h_1\sqrt{(\xi^2 - q^2)} + \frac{1}{q^2}h_2\sqrt{(\xi^2 - q^2)} + \frac{1}{q^4}h_3\sqrt{(\xi^2 - q^2)}]$$

$$h_1(q) = \frac{\gamma}{q}\int_0^D J_1(zq)\left[\frac{z\,(D-z)^2}{3}(2D + z) + 2\,z\,\hat{D}\,(\hat{D} - D)\,(D - z)\right] dz$$

$$h_2(q) = \frac{2\,\gamma}{q}\int_0^D J_1(zq)\, z\,(D - 2z)\, dz$$

$$h_3(q) = -\frac{2\,D\,\gamma}{q}\, J_1(Dq)$$

$$\gamma = \left[\frac{D^4}{4} + D^2\,\hat{D}\,(\,\hat{D} - D)\right]^{-1}$$

and $J_1(\ )$ represents a Bessel function of first kind, of order 1.

We next assume that D is large, i.e., that the light has propagated through many correlation lengths of the medium. Then (16) may be simplified to

$$\frac{-3S(q)}{2\{1 + 3\,\delta\,(1+\delta)\}D^3q^3} = \int_0^\infty q\,\frac{S'(\sqrt{\xi^2 + q^2}}{\sqrt{\xi^2 + q^2}}d\xi \tag{17}$$

where S' denotes $\frac{\partial S}{\partial\xi}$ and $\delta = \frac{\hat{D}}{D} - 1$. The three-dimensional power spectrum of the medium is now given by

$$S_3(q) = 4\frac{\pi}{q}\int_0^\infty \rho\sin(\rho q)\bar{R}(\rho)d\rho) \tag{18}$$

where $\bar{R}(\rho) = \beta R(\rho)$, the normalized correlation function of the medium, is the Hankel transform of S(q). Substitution into (18) yields, after some manipulation

$$S_3(q) = \frac{6\,\pi\,S_1(q)}{[1 + 3\delta(1+\delta)]D^3q^4} \tag{19}$$

Thus the 3-D spectrum of the medium can be obtained from the 2-D spectrum of the image by simply dividing each spectral component by the value of the frequency raised to the fourth power and a scaling factor that is determined by the geometry of the scattering configuration.

III. EXPERIMENTAL APPARATUS

The experimental facility referred to here as the turbulent mixer , was designed and built by one of us (Hesselink,1977 a, Ref 6) for the study of the propagation of a weak shock wave through a random medium (Hesselink and Sturtevant, Ref 7). The turbulent mixer , shown in Figure 2 mounted at the end of the *GALCIT*[*] 43-cm diameter shock tube , generates a 26.7 cm square by 35 cm long rectangular volume of incompletely mixed gas. The apparatus consists of an array of fine jets alternately of helium and freon-12 (CCl_2F_2) in a checkerboard configuration behind coarse grids located on opposite sides of a box. The grids are rapidly retracted flush with the sidewalls before the shocktube is fired. The other two sidewalls are fitted with optical windows for diagnostics. The vertical upstream and downstream walls of the box are fitted with shutters which can be opened rapidly just before shock arrival. This process is automated and the arrival time of the shock relative to the decay time of the turbulent density field can be varied. The gas mixture can be made neutrally buoyant so that the mean interface between the scattering region and the uniform gas in the shocktube remains parallel to

[*] Graduate Aeronautical Laboratories California Institute of Technology

the plane of the incoming wave. The mean speed of sound in the mixture is matched to that of air surrounding the scattering region to minimize perturbations on the shock caused by the mean properties of the medium. In this paper we report on the propagation of laser radiation through the random medium in the absence of a shock wave. The studies are performed at a time in the decay process that corresponds to the time used in the shock scattering experiments.

The optical configuration used in the experiments is shown in Figure 1. A beam expander consisting of lens L1 and L2 expands the output of an argon ion laser (Spectra-physics 165-08) into a 15 cm diameter beam. The plane, monochromatic wave of wavelength $\lambda = 5145$ Å is normally incident upon the random medium. The transmitted radiation is stored on film at the shadowgraph plane using no imaging optics. The still photographs are recorded at different distances $\hat{D}$ from the scattering medium using Kodak Tri-x-pan professional sheet film (4x5) and the film is developed in microdol-x under standard development conditions. The exposure time is 1 msec, a period short enough to freeze the motion of the gas in the box in the absence of a shock wave. The developed negatives are digitized on a Perkin Elmer PDS microdensitometer, model 1010 A, and the digital data are stored on magnetic tape for later processing. The digital data can also be synthesized into a photograph using a laser printing device.

IV. RESULTS

4.1 Discussion

Propagation of radiation between planes z=0 and $z=\hat{D}$ is considered to be a two stage process. First, the propagation through the random medium is analyzed and a simple relationship between the two-dimensional image spectrum and the three-dimensional spectrum of the index of refraction field exists, given by equation (19).

Second, the output wavefield that results at z = D is propagated through free space over a distance $d = \hat{D} - D$. The analysis shows that for a given spectrum of the medium each component of the image spectrum is multiplied by a scaling factor, which is determined by the geometry of the experimental configuration. In other words, the image spectra obtained at different downstream locations are related to each other by a constant shift along the ordinate, when plotted on log-log paper.

To test the validity of the analytical results a sequence of eleven still photographs have been taken at two different distances $d = \hat{D} - D = 52$ cm and $d = 102$ cm (see Figure 1) downstream of the random medium. Representative photographs of the kind that have been analyzed are shown in Figure 3. The propagation distances are $d = 52\ cm$ for the photograph on the left and $d = 102\ cm$ for the photograph on the right ; both pictures are reconstructions from the digital data that have been obtained by scanning a 5.12 x 5.12 cm square section of the original negative. The pixel (picture element) size used for the scan is 100 μm x 100 μm and the probability density function (pdf) of the film density is shown just below the picture. The scanner has eight bit grey scale resolution and low numbers on the abscissa correspond to white in the photograph and large numbers represent black. The exposure of the photographs has been carefully controlled to insure operation within the linear range of the Hurter-Driffield curve. The dynamic range of the digitizer is adjusted such that it just spans the full extent of the recorded density fluctuations. A qualitative observation of the representative photographs in Figure 3, reveals that the contrast of the image increases with increasing d as manifested by the broadening of the image histogram. Furthermore, more pronounced fringes are visible adjacent to the brightest lines in the picture on the right than in the one on the left. These patterns are interpreted to be cross sections of a, not fully developed, caustic network. Before elaborating more on the

significance of the appearance of caustics in the images, and their relevance for the calculation of the spectrum of the medium, the results will be discussed first.

4.2 Scaling Factor

The ensemble averaged results obtained at the two measuring stations are shown in Figure 4. The top graph on the left shows the power spectral density of the image recorded at d=52 cm and the right top graph represents the results for the measurements at d=102 cm. From these data the three-dimensional medium spectrum can be obtained using equation (19) and the result are shown in the two bottom graphs in the same figure. The experimentally determined error bound gives rise to an uncertainty in the vertical position of the data points equal to approximately two times the size of the circles used in the graphs. The two graphs coincide when plotted in the same coordinate system, which indicates that the scaling factor $\frac{1}{1 + 3\delta(1 + \delta)}$ correctly accounts for the propagation through free space. Furthermore, the appearance of caustics in the photographs obtained at the measuring station farthest downstream do not seem to effect the determination of the power spectrum of the medium. Thus a very simple procedure can be followed to compute the 3-D power spectral density of the medium from the image power spectral density function ; each spectral component of the image psd is divided by q^4 ,the wavenumber to the fourth power,and the result is multiplied by a scale factor which depends on the free space propagation between the medium and the recording film plate.

It is interesting to compare the results with published data on velocity spectra in homogeneous and isotropic turbulent media. In Figure 4 two lines with slope -9 and -11/3 are drawn for comparison. Of course, these straight lines with the indicated coefficients are not the only lines that can be fitted to the data with some degree of

accuracy, but they are merely plotted to indicate that the data seem to fit these curves rather well. The cross-over point between the two lines occurs at a frequency of 5.7 cycles/cm, which corresponds to a length scale in the medium of 1.7 mm. The region to the right of this point represents the viscous subrange and the region to the left indicates the inertial subrange.

4.3 Noise Considerations

In the analog mathematical representation the spectrum of the medium is related to the correlation function by a Fourier Transform operation as shown in Section II. In practice, the digital data are contaminated with noise and the accuracy of the numerical procedure has to be considered. The analysis shows that the value of the correlation function for large arguments depends very crucially on the shape of the spectrum at low frequencies. However, this portion of the spectrum is not known accurately for two reasons. First, according to the sampling theorem the lowest frequency that can be obtained corresponds to a length scale of half the size of the scanned area in the photograph; the power associated with those scales is not measured very precisely because of the rather limited cycles over which the data can be averaged. Therefore, in our case, the value of the correlation function for arguments larger than approximately a few centimeters cannot be computed with good accuracy from the medium spectrum. Second, in order to compute the 3-D spectrum of the medium from the 2-D spectrum of the photograph, each component of the latter has to be divided by the frequency to the fourth power. This procedure introduces large errors in the presence of noise. For instance, consider S_R to be the true value of the spectrum and ΔS to be additive noise.Furthermore, let the measured image spectrum be represented by $S_M = S_R + \Delta S$ and S denotes the true 3-D spectrum of the medium. The result of the analysis shows

that

$$S_M = S_R + \Delta S = \alpha\, q^4\, S + \Delta S \tag{20}$$

where α denotes a proportionality constant and

$$S_{III} = S_M / q^4 = S + \Delta S / q^4 \tag{21}$$

However, S is bounded when q approaches 0, and therefore the error in S_{III}, the 3-D medium spectrum, increases without bound. In the present experiments care is taken to reduce the noise in the low frequency data by subtracting from the shadowgraph data a reference picture that corresponds to the background noise in the system; this picture is obtained by exposing a piece of film in the absence of any density fluctuations in the turbulent mixer. The "no flow" photographs are taken just before the actual data are collected and all negatives are developed under identical conditions, then digitized and finally the images are subtracted digitally. The photographs with the background noise substantially reduced are subsequently used for computing the image power spectral density and the medium 3-D psd. In addition to these experimental sources of error, in the theoretical analysis we make the assumption that the radiation propagates over a distance of many scale lengths. This assumption is not valid for small frequencies q or large length scales in the medium.

The difficulty associated with the limited data base can be alleviated by averaging over a larger ensemble, but the difficulty associated with the division by q^4 is inherent to the method. This factor arises from equation (7), where the second derivative of the fluctuating index of refraction field is integrated over the path length. This second derivative is directly related to the q^4 factor in the expression for the spectrum (19). It is possible that some of the difficulties may be reduced if a schlieren or interferometry recording configuration is used, because these methods are sensitive to the derivative of the index of refraction field integrated over the path length and the optical path length,

respectively.

4.4 Caustic Networks

The appearance of bright lines in the shadowgraphs, in particular in the photographs taken at d = 102 cm, suggest that regions of high light intensity are found outside the scattering medium. These regions of high intensity, flanked on one side by Airy - type fringes are generally known as caustics, and the collection of caustics as a caustic network. Berry and Upstill have recently reviewed the properties of caustic networks from the view point of catastrophe theory [Ref. 7]. They indicate that caustic networks often contain caustic line pairs. In our photographs we note bright lines decorated on one as well as on both sides by fringe patterns. These bright lines are tentatively interpreted as being caustics or caustic pairs; a caustic pair may appear as a double bright line or as a single line (a double line blurred by diffraction) flanked on both sides by fringes. This interpretation suggests that the caustic network is not yet fully developed, in the sense that the scintillation index of the intensity field, determined at the two measuring stations, has not yet peaked; a maximum should then occur at a further distance downstream of the scattering media. These matters have been discussed by several authors.

Hesselink (Ref. 8) has discussed the formation of caustics **inside** the random medium. He considered an initial plane wave incident on a random medium and computed the probability density function for the distance to first focus as measured along a ray using a Monte Carlo simulation and Kulkarny and White (Ref. 9) have computed the same function theoretically; this function very sharply peaks at a non- dimensional distance of s = 1.4, where s is given by

$$s = \epsilon^{2/3} \sigma^{2/3} z \qquad (23)$$

and

$$\sigma^2 = 6 \int_0^\infty 1 - \frac{\partial}{\partial r}\frac{[1}{r}\frac{\partial}{\partial r}] R(r)\ dr \tag{24}$$

where R represents the correlation function of the scattering medium. These results are obtained for 2-D wave propagation, but recent 3-D calculations indicate that equations 23 and 24 are approximately correct for the three-dimensional problem as well [Ref 10]. The distance s= 1.4 can be interpreted to be the most probable focal length f' in the medium and for a medium which is described by a Gaussian correlation function

$$R = e^{-\frac{r^2}{2\ell^2}} \tag{25}$$

the expression for f' is

$$f' = .7146 \frac{l}{\epsilon^{2/3}} \tag{26}$$

On the basis of (27) the smallest scales, for which $l = 1$ mm will focus over a distance $f' = 73.5$cm and larger scales beyond that distance. Thus caustic formation could occur for the smallest scales near z = D, but larger scales would tend to focus outside the random medium. Figure 5 shows a shadowgraph obtained at z = D. The photograph shows some structure, but with rather low contrast. Beyond z= D the wavefront propagates deterministically and along a ray the difference of the two principal radii of curvature of the wave ,$R_1 - R_2$, remains constant. A complex three-dimensional caustic network is formed characterized by topological features which are directly determined by the wavefront at z = D.

Several authors have considered the propagation beyond a thin phase screen. Buckley (Ref. 10, 11) considers an initially plane wave incident on a thin phase screen, and computes the diffracted wave field beyond the phase screen in case strong rms phase fluctuations, typically larger than 1 rad, are introduced by the screen. He computes the

scintillation index as a function of the downstream distance from the screen and shows that eddies in the inertial subrange are responsible for the intensity scintillations in the region of a fully developed caustic network, that is, where the scintillation index attains a maximum. An estimate of the location where caustics are first found outside the random medium in our experiments is readily obtained from Buckley's or Taylor's analysis (Ref. 3). Taylor showed that for a slab medium of thickness D characterized by a Gaussian correlation function $C(r) = e^{-r^2/\ell^2}$ the distance to first focus, as measured from the exit plane, is determined by

$$d_{focus} = [\{1 / 8(\pi)^{1/2}\} \ell^3 / D <\epsilon^2>]^{1/2} \tag{27}$$

Upon substitution of the numerical values presented in (5) and assuming a value of $l =$ 1.5 mm the distance $d_{focus} = 1.0$ m. Perturbations of longer spatial extent, for instance $l = 1.5$ cm, tend to focus at a distance of $d_{focus} = 31.6$ m.

Thus, these calculations suggest that for our experiments, in which eddies in the inertial subrange are characterized by length scales between l = 1.5 mm and l = 1.5 cm, the fully developed caustic region occurs farther downstream, beyond d = 102 cm, the measuring location for the photograph in Figure 3. These arguments further substantiate that the bright lines shown in the shadowgraphs, decorated on both sides by fringes , constitute a partially developed caustic network. The results of the perturbation analysis presented here, including the scale factor shown in equation (19), is thus valid in the near region of the scattering medium, and has been tested for $\delta \leq 3$. This region of validity compares to region (a) in Buckley's analysis, namely:

$$z \leq \frac{kL_2L_4}{\phi_0}$$

where

$$L_n^{-n} = \left(-\frac{1}{r}\frac{\partial}{\partial r} r \frac{\partial}{\partial r}\right)^{\frac{1}{r}n} \left(R(r)\right)|_{r=0} \tag{28}$$

n=2 *or* 4 and ϕ_0 represents the phase fluctuation at z=D.

In the fully developed caustic regime the intensity fluctuation will scale differently with d and D and has been studied by Berry (Ref. 12), Buckley (Ref. 10,11) and Jakeman and McWhirter (Ref. 13). The statistics of the topology of the fully developed caustic pattern has been studied by Longuet Higgins (Ref. 14, 15, 16 and 17) and by Berry and Upstill (Ref. 7). Kratsov (ref. 18) also discusses the probability of formation of caustics, but it is unlikely that perturbation analysis is valid in this region.

V. CONCLUSIONS

The medium 3-D power spectral density function can be obtained from the image 2-D power spectral density of a shadowgraph photograph by dividing each frequency component of the latter by the frequency to the fourth power. The result, equation (19) is applicable in the near region of the random medium defined by equation (27) or (28). In this regime the caustic network is possibly not fully developed. The correlation function cannot be accurately computed from the power spectral density function, unless the low frequency end of the spectrum is obtained very precisely using a large ensemble average. The non intrusive diagnostic technique described here is applicable even if a partially developed caustic network is formed at the measuring station.

VI. ACKNOWLEDGEMENT

Helpful discussions with Professor B.Sturtevant are gratefully acknowledged. The assistance of D. Madura with the numerical calculations is greatly appreciated. This research was in part supported by the Caltech President's Fund (PF-154) the National Science Foundation (CME-7822089) and NASA-Ames (NAS 2-83).

VII.REFERENCES

1. Brown, G.L. and Roshko, A.,J.Fluid Mech. 64, 775, 1974

2. Uberoi, M.S. and Kovasznay, L.S.G. J Applied Phys. 26, 1954

3. Taylor, L.S., AIAA Journal 8, 1284, 1969

4. Tatarski, V.I., *Wave Propagation In A Random Medium*, Mc Graw-Hill, New York, 1960

5. Whitham, G.B., *Linear* and *Nonlinear Waves*, John Wiley, New York, 1974.

6. Hesselink,L., Proceedings 11th International Symposium on Shock Tubes and Waves, Seattle, Wa., July 1977

7. Berry and Upstill. Progress in Optics 18: 257, 1980.

8. Hesselink, L., in preparation for the Journal of Fluid Mechanics; Sturtevant, B , Hesselink, L ,White , B.S., Kulkarny V. and Catherasoo, C. Propagation of Shock Waves through Nonuniform and Random Media, Proceedings of the 13 th International Symposium on Shock Tubes and Waves, July 1981, Niagara Falls, New York.

8. Kulharry, V. and White, B.S. To appear in Physics of Fluids.

9. White, B.S., The Stochastic Caustic, to be submitted to SIAM, Journal of Appl. Math.

10. Buckley, R, Aust. J. Phy. 24:351-371, 1971.

11. Buckley, R. Aust. J. Phys., 24:373-396, 1971.

12. Berry, M.V. J. Phys. A. Math. Gen. 10: no. 12, 2061, 1977.

13. Jakeman, E. and McWhirter, J.G. J. Phys. A. Math. Gen., 10: no. 9, 1599, 1977.

14. Longuet-Higgins, M.S. J.O.S.A. 50, no. 9, 838, 1960.

15. Longuet-Higgins, Proc. Comb. Phil. Soc. 54:439, 1958.

16. Longuet-Higgins, Proc. Comb. Phil. Soc. 54:91, 1951.

17. Longuet-Higgins, Proc. Comb. Phil. Soc. 54:27, 1960.

18. Kratsov, Y.A. Soviet Phy. Jetp, 2d, 3, 413, 1969.

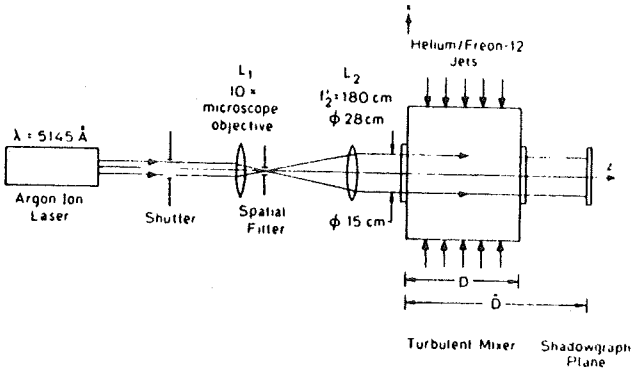


Fig. 1. Optical configuration.

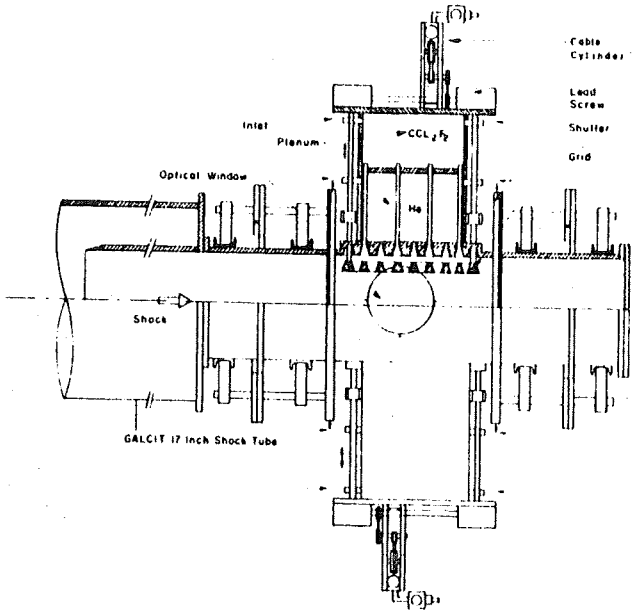


Fig. 2. Experimental apparatus for generating the random medium.

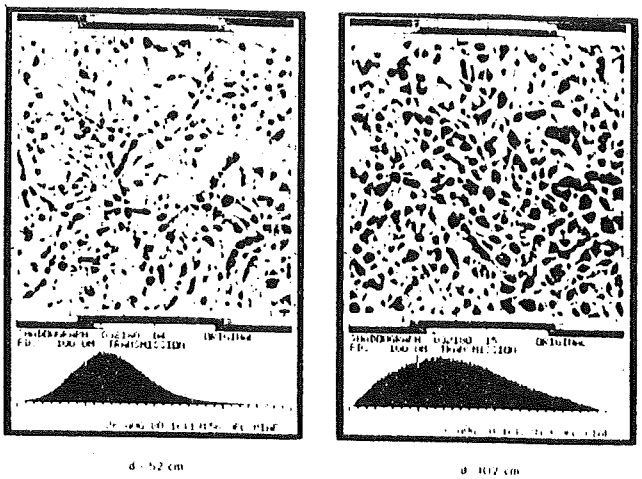


Fig. 3. Representative shadowgraph photographs.

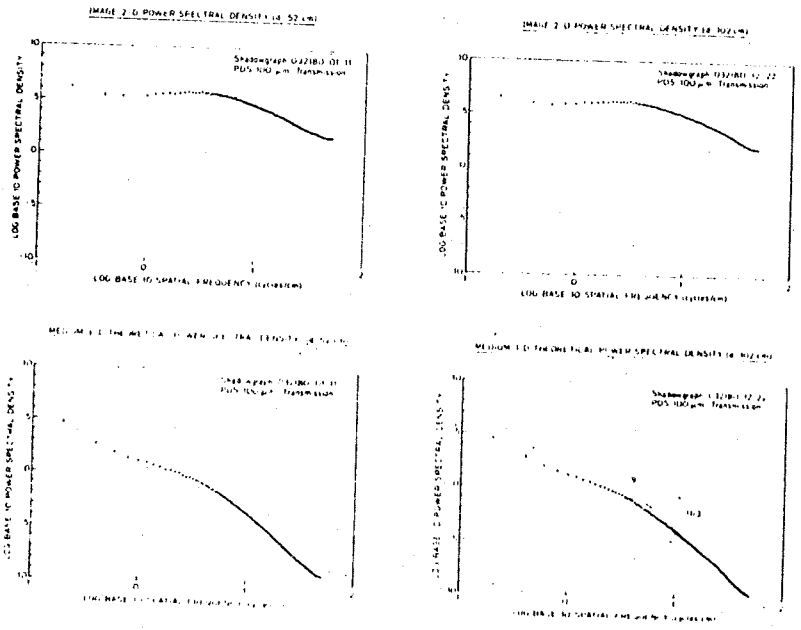


Fig. 4. Power spectral density curves.

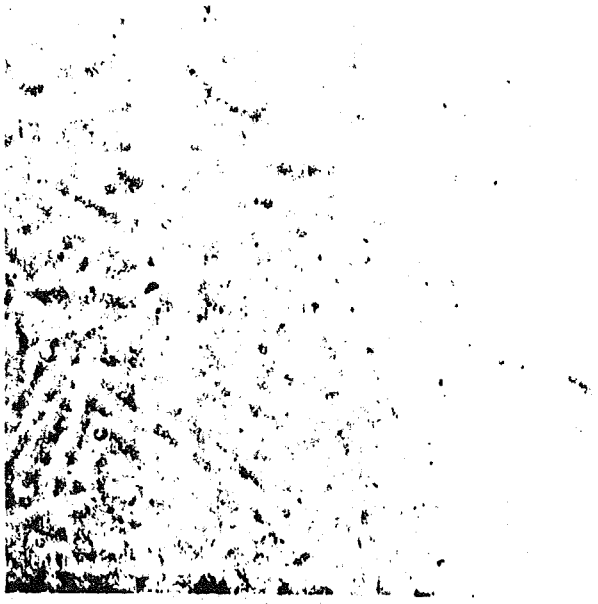


Fig. 5. Shadowgraph photograph obtained at the exit window (background noise not removed).